Cardiac electrical defects in progeroid mice and Hutchinson–Gilford progeria syndrome patients with nuclear lamina alterations

José Rivera-Torres[a,1], Conrado J. Calvo[a,b,c,2], Anna Llach[d,2], Gabriela Guzmán-Martínez[a,e,2], Ricardo Caballero[f], Cristina González-Gómez[a], Luis J. Jiménez-Borreguero[a,g], Juan A. Guadix[h,i], Fernando G. Osorio[j], Carlos López-Otín[j], Adela Herraiz-Martínez[d,k], Nuria Cabello[d,k], Alex Vallmitjana[l], Raul Benítez[l], Leslie B. Gordon[m,n,o], José Jalife[a,p,q], José M. Pérez-Pomares[h,i], Juan Tamargo[f], Eva Delpón[f], Leif Hove-Madsen[d,k], David Filgueiras-Rama[a,r], and Vicente Andrés[a,3]

[a]Centro Nacional de Investigaciones Cardiovasculares Carlos III (CNIC), 28029 Madrid, Spain; [b]Group Electrophysiology and Bioengineering (GEB), Information and Communication Technologies Institute (ITACA), Universitat Politècnica de València, 46022 Valencia, Spain; [c]Department of Physiology, Facultad de Medicina y Odontología, Universidad de Valencia, 46010 Valencia, Spain; [d]Institut de Investigació Biomedica Sant Pau, Hospital de Sant Pau, 08025 Barcelona, Spain; [e]Cardiac Imaging Unit, Cardiology Department, Hospital Universitario La Paz, IdiPaz, 28046 Madrid, Spain; [f]Department of Pharmacology, School of Medicine, Universidad Complutense, 28040 Madrid, Spain; [g]Servicio de Cardiología, Hospital de la Princesa, 28006 Madrid, Spain; [h]Department of Animal Biology, Instituto de Investigación Biomédica de Málaga (IBIMA), University of Málaga, 29071 Málaga, Spain; [i]Centro Andaluz de Nanomedicina y Biotecnología (BIONAND), Junta de Andalucía, Universidad de Málaga, 29590 Campanillas, Spain; [j]Departamento de Bioquímica y Biología Molecular, Instituto Universitario de Oncología, Universidad de Oviedo, 33006 Oviedo, Spain; [k]Cardiovascular Research Center, Hospital de Sant Pau, 08025 Barcelona, Spain; [l]Automatic Control Department, Universitat Politécnica de Catalunya, 08034 Barcelona, Spain; [m]Department of Pediatrics, Alpert Medical School of Brown University, Providence, RI 02903; [n]Department of Pediatrics, Hasbro Children's Hospital, Providence, RI 02903; [o]Department of Anesthesia, Division of Critical Care Medicine, Boston Children's Hospital and Harvard Medical School, Boston, MA 02115; [p]Department of Internal Medicine, University of Michigan, Ann Arbor, MI 48109; [q]Center for Arrhythmia Research, University of Michigan, Ann Arbor, MI 48109-2800; and [r]Department of Cardiology, Cardiac Electrophysiology Unit, Hospital Clínico San Carlos, 28040 Madrid, Spain

Edited by J. G. Seidman, Harvard Medical School, Boston, MA, and approved October 3, 2016 (received for review March 8, 2016)

Hutchinson–Gilford progeria syndrome (HGPS) is a rare genetic disease caused by defective prelamin A processing, leading to nuclear lamina alterations, severe cardiovascular pathology, and premature death. Prelamin A alterations also occur in physiological aging. It remains unknown how defective prelamin A processing affects the cardiac rhythm. We show age-dependent cardiac repolarization abnormalities in HGPS patients that are also present in the *Zmpste24*$^{-/-}$ mouse model of HGPS. Challenge of *Zmpste24*$^{-/-}$ mice with the β-adrenergic agonist isoproterenol did not trigger ventricular arrhythmia but caused bradycardia-related premature ventricular complexes and slow-rate polymorphic ventricular rhythms during recovery. Patch-clamping in *Zmpste24*$^{-/-}$ cardiomyocytes revealed prolonged calcium-transient duration and reduced sarcoplasmic reticulum calcium loading and release, consistent with the absence of isoproterenol-induced ventricular arrhythmia. *Zmpste24*$^{-/-}$ progeroid mice also developed severe fibrosis-unrelated bradycardia and PQ interval and QRS complex prolongation. These conduction defects were accompanied by overt mislocalization of the gap junction protein connexin43 (Cx43). Remarkably, Cx43 mislocalization was also evident in autopsied left ventricle tissue from HGPS patients, suggesting intercellular connectivity alterations at late stages of the disease. The similarities between HGPS patients and progeroid mice reported here strongly suggest that defective cardiac repolarization and cardiomyocyte connectivity are important abnormalities in the HGPS pathogenesis that increase the risk of arrhythmia and premature death.

Hutchinson–Gilford progeria syndrome | progerin | prelamin A | connexin43 | calcium handling

The *LMNA* gene encodes A-type lamins (lamin A and lamin C), key components of the mammalian nuclear envelope with important structural and regulatory functions that affect signaling, transcription, and chromatin organization among other processes (1). Mature lamin A is produced from the precursor prelamin A through a series of posttranslational modifications, consisting of sequential farnesylation at the cysteine in the Cysteine-Serine-Isoleucine-Methionine motif, cleavage of the Serine-Isoleucine-Methionine residues, carboxymethylation of the newly accessible cysteine, and a final proteolytic cleavage by the zinc metallopeptidase STE24 (ZMPSTE24, also called FACE-1) (2).

Mutations in the human *LMNA* gene or defective processing of prelamin A cause a group of diseases termed laminopathies, including the premature aging disorder Hutchinson–Gilford progeria syndrome (HGPS), a very rare genetic disorder with an estimated prevalence of 1 in 21 million people (www.progeriaresearch.org).

Significance

Defective prelamin A processing causes cardiovascular alterations and premature death in Hutchinson–Gilford progeria syndrome (HGPS) patients and also occurs during physiological aging. We found overt repolarization abnormalities in HGPS patients at advanced disease stages. Similar alterations were present in progeroid *Zmpste24*$^{-/-}$ mice, which had cardiomyocytes that exhibited prolonged calcium transient duration and reduced sarcoplasmic reticulum calcium loading capacity and release, consistent with absence of isoproterenol-induced ventricular arrhythmias. *Zmpste24*$^{-/-}$ mice developed age-dependent bradycardia and PQ interval/QRS complex prolongation, likely contributing to premature death. These defects correlated with mislocalization of connexin43, which was also noted in heart tissue from HGPS patients. These results reveal molecular alterations that might cause cardiac rhythm alterations and premature death in HGPS.

Author contributions: J.R.-T., R.C., J.J., J.T., E.D., L.H.-M., D.F.-R., and V.A. designed research; J.R.-T., C.J.C., G.G.-M., R.C., C.G.-G., L.J.J.-B., J.A.G., A.H.-M., N.C., A.V., R.B., J.M.P.-P., J.T., and L.H.-M. performed research; J.R.-T., C.J.C., A.L., G.G.-M., R.C., L.J.J.-B., F.G.O., L.B.G., J.M.P.-P., J.T., E.D., L.H.-M., D.F.-R., and V.A. analyzed data; C.G.-G. generated and maintained mice and cells; F.G.O. and C.L.-O. generated and maintained mice; V.A. coordinated the study; and J.R.-T., C.J.C., C.L.-O., L.B.G., J.J., J.M.P.-P., E.D., L.H.-M., D.F.-R., and V.A. wrote the paper.

The authors declare no conflict of interest.

This article is a PNAS Direct Submission.

Freely available online through the PNAS open access option.

[1]Present address: Faculty of Biomedical Science, European University of Madrid, 28670 Villaviciosa de Odón, Madrid, Spain.

[2]C.J.C., A.L., and G.G.-M. contributed equally to this work.

[3]To whom correspondence should be addressed. Email: vandres@cnic.es.

This article contains supporting information online at www.pnas.org/lookup/suppl/doi:10.1073/pnas.1603754113/-/DCSupplemental.

HGPS patients exhibit accelerated atherosclerosis and arterial stiffness, leading to premature death at an average age of 14.6 y, predominantly from myocardial infarction, heart failure, or stroke (3, 4). Most HGPS patients carry a noninherited de novo heterozygous synonymous mutation in the *LMNA* gene (c.1824C > T: GGC > GGT; p.G608G), which activates the use of an internal 5′ splicing site in exon 11 that causes the synthesis of progerin. This unprocessed form of prelamin A lacks 50 amino acids encompassing the ZMPSTE24 cleavage site and therefore, remains permanently farnesylated (2). *ZMPSTE24* mutations have also been linked to several other human progeroid syndromes (5, 6), reinforcing the notion that accumulation of progerin or prelamin A accelerates cellular aging. Moreover, progerin and prelamin A are both expressed in cells and tissues of normally aging non-HGPS individuals, suggesting their involvement in physiological aging (reviewed in refs. 2 and 7).

Genetically modified mice expressing prelamin A or progerin have enabled the study of mechanisms underlying progeria (8) and testing of the efficacy of various therapies (9, 10). Here, we examined cardiac electrical alterations in 15 HGPS patients with the classical *LMNA* c.1824C > T mutation, representing ∼5% of the world population (www.progeriaresearch.org). We then correlated the observed alterations in HGPS patients to the underlying molecular processes in *Zmpste24*-null mice; these mice accumulate farnesylated prelamin A in the nuclear envelope and phenocopy several other defects observed in HGPS, including cardiovascular alterations and premature death (average lifespan ∼20 wk vs. >2 y in WT mice) (9, 11).

Results

Electrocardiographic Alterations in HGPS Patients. *SI Appendix*, Tables S1 and S2 show electrocardiographic measurements from HGPS patient carriers of the *LMNA* c.1824C > T mutation (n = 15, age range 2–19 y old) and controls (n = 13, age range 4–19 y old), respectively. A glossary of electrocardiographic parameters can be found in *SI Appendix*. As they aged, seven patients showed overt repolarization abnormalities in at least one electrocardiogram (ECG) that were compatible with coronary artery disease (ST segment depression/elevation and negative and biphasic T waves) (a representative example is in *SI Appendix*, Fig. S1*A*). One patient showed significant QTc interval prolongation (537 ms) in the context of ischemia at advanced stages of the

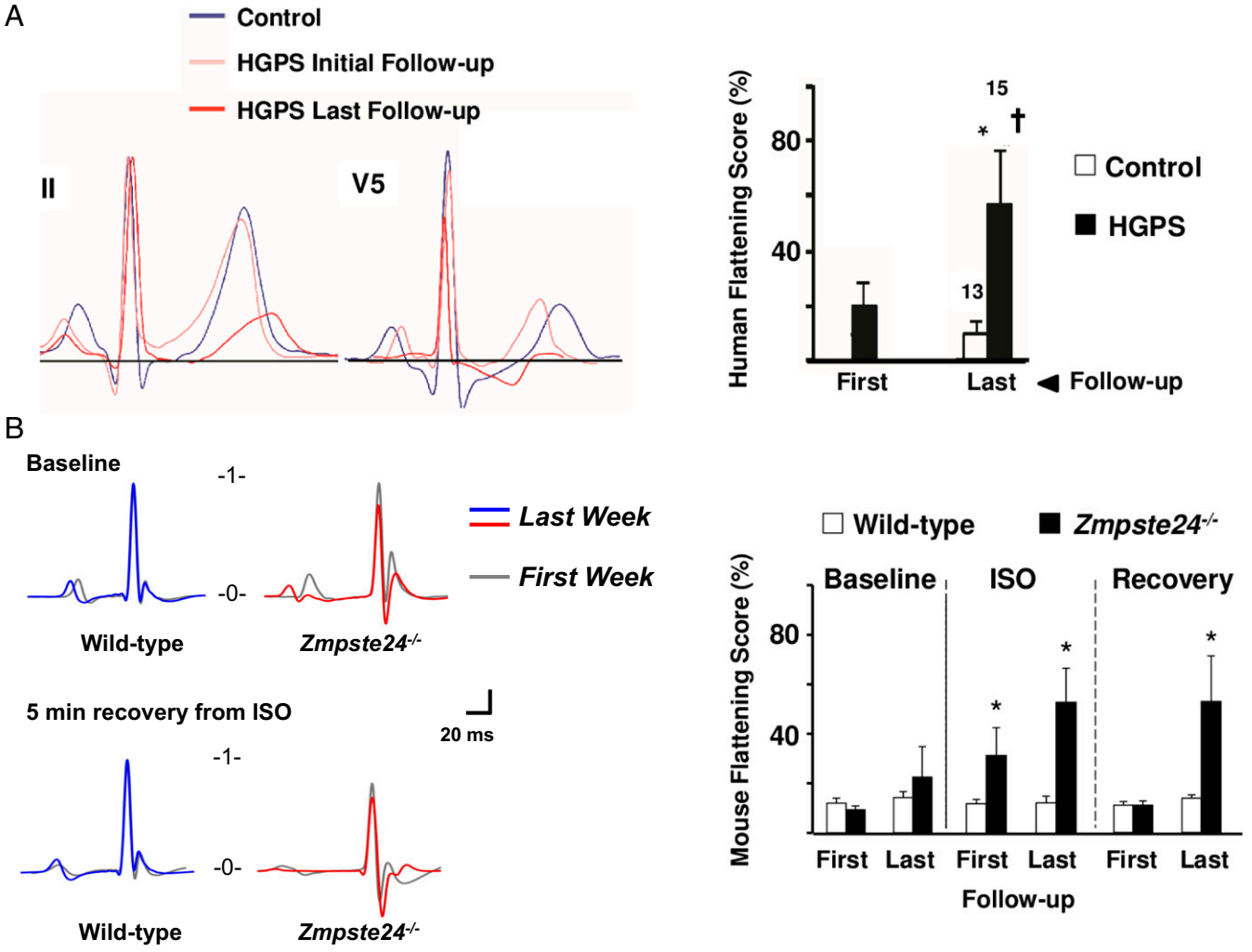

Fig. 1. Age-related exacerbation of repolarization abnormalities in HGPS patients and *Zmpste24*$^{-/-}$ mice. (*A*, *Left*) Extracted averaged ECG leads II and V5 from human control participants (blue traces) and HGPS patients at initial stage (Initial; light red trace) and advanced stages (Last; dark red trace). (*A*, *Right*) Quantification of mean flattening scores. (*B*, *Left*) Representative T-wave abnormalities in *Zmpste24*$^{-/-}$ mice comparing the first and the last isoproterenol (ISO) challenge (*SI Appendix, SI Materials and Methods*). (*B*, *Right*) Mean effective flattening scores at baseline, after ISO exposure and during 5-min recovery. *P < 0.05 vs. control; $^{\dagger}P$ < 0.05 vs. first follow-up. First: 11-wk-old mice; Last: 19-wk-old mice or last week before death.

disease (18 y of age). These alterations were not observed in controls (a representative example is in *SI Appendix*, Fig. S1*B*). Repolarization abnormalities in HGPS patients were highly evident at advanced disease stages. Compared with age-matched controls, HGPS patients exhibited significant T-wave flattening, which was exacerbated as disease progressed (Fig. 1*A*, initial: initial ECG; last: last ECG during follow-up). All patients and controls had sinus rhythm and normal PR interval and QRS complex duration (*SI Appendix*, Tables S1 and S2). Interestingly, although all HGPS patients exhibited cardiac rhythm within physiological values, the heart rate and PR interval tended to be slower and larger, respectively, in older HGPS patients (6 of 15) at the end of the follow-up period (26.8 ± 2.3 mo follow-up): heart rates on first and last ECGs were 114 ± 7 and 101 ± 7 beats per minute (bpm), respectively, $P = 0.36$; PRs on first and last ECGs were 115 ± 2 and 128 ± 11 ms, respectively, $P = 0.22$.

Time Course of ECG Abnormalities in Progeroid *Zmpste24*$^{-/-}$ Mice. We next analyzed the electrocardiographic phenotype of *Zmpste24*$^{-/-}$ mice, an established preclinical model of HGPS (9, 11). A glossary of electrocardiographic parameters can be found in *SI Appendix*. To study repolarization, we quantified T-wave flattening by measuring T-wave morphology changes, including sharpness, by excess kurtosis of the T-wave peak in relation to its geometrical change from the isoelectric line and the area under the T wave (*SI Appendix*, *SI Materials and Methods*). Similar to HGPS patients, progeroid mice showed repolarization abnormalities manifested as significant T-wave flattening. To determine the risk of ventricular arrhythmia associated with T-wave alterations, we used the β-adrenergic agonist isoproterenol, which can trigger calcium-related alterations in cardiac repolarization. Weekly isoproterenol challenge, based on its sympathomimetic effect and ability to induce Ca^{2+}-related alterations in repolarization, further exacerbated the repolarization alterations as *Zmpste24*$^{-/-}$ mice aged, although acute isoproterenol did not cause significant ventricular arrhythmias in *Zmpste24*$^{-/-}$ or controls (Fig. 1*B*). Although both groups responded normally in the first week of follow-up, older *Zmpste24*$^{-/-}$ mice developed a very marked reduction in the heart rate (bradycardia) during recovery from isoproterenol (Fig. 2*A*). In addition, compared with WT controls, *Zmpste24*$^{-/-}$ mice progressively developed longer RR intervals as they aged (Fig. 2 *B* and *C*). The variability of the RR interval, measured as the SD, increased linearly as a function of the average RR interval (*SI Appendix*, Fig. S2) and was associated with increased incidence of premature ventricular complexes (Fig. 2*D* and *SI Appendix*, Fig. S3) and a short lifespan.

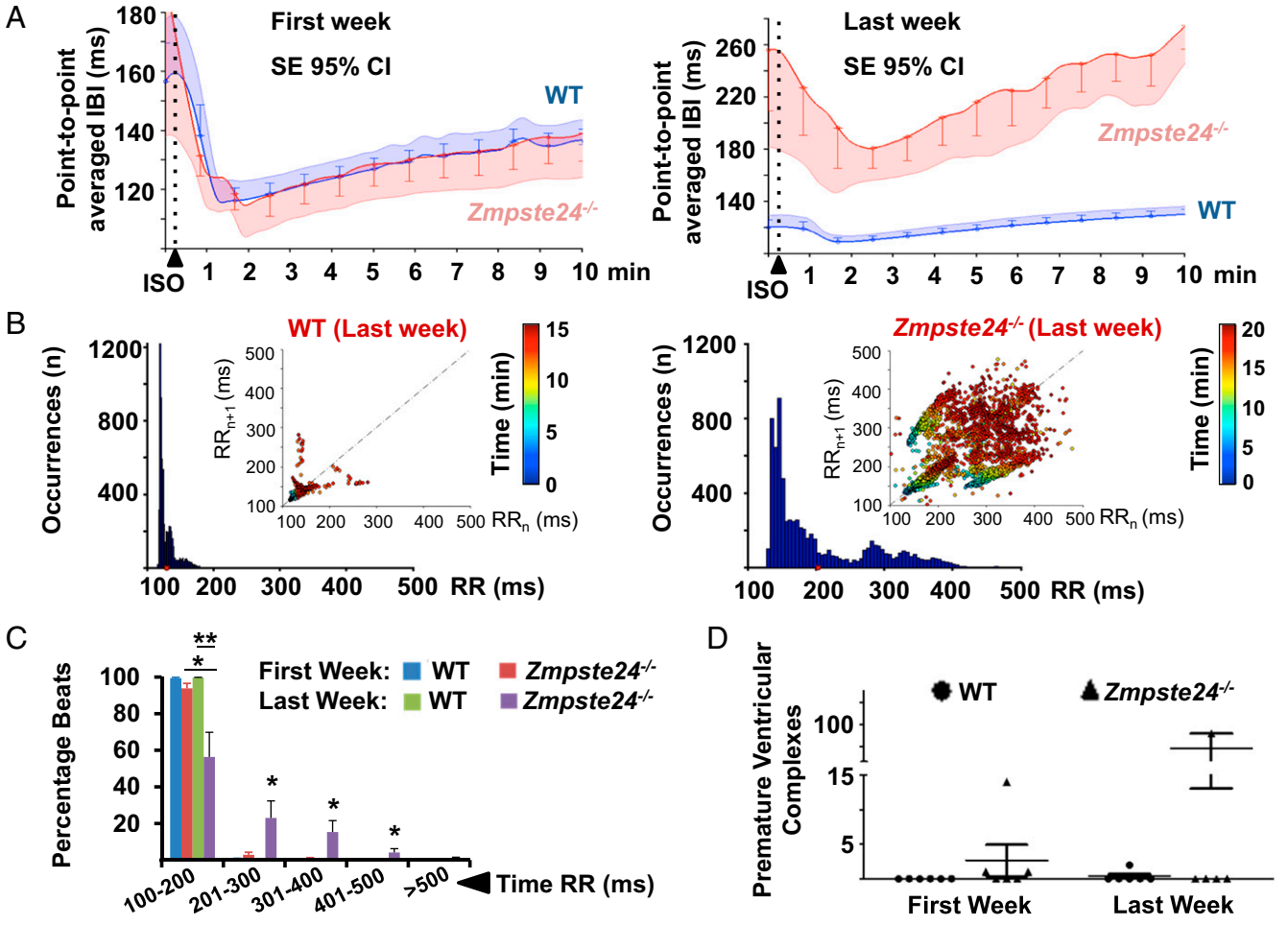

Fig. 2. Severe bradycardia in postisoproterenol (post-ISO) administration recovery is associated with an increase in premature ventricular complexes in *Zmpste24*$^{-/-}$ mice. First: 11-wk-old mice; Last: 19-wk-old mice or last week before death. (*A*) β-Adrenergic response [interbeat interval (IBI)] in WT and *Zmpste24*$^{-/-}$ mice from the first to the last ISO challenge. 95% CI, 95% confidence interval. (*B*) RR histograms in WT and *Zmpste24*$^{-/-}$ mice during ISO time course challenge. The *Insets* show correlation plots between consecutive cardiac beats (RRn vs. RRn + 1; *n* = cardiac beat number within the entire registration period; color-coded timescale). A significant increase in the percentage of long RR intervals during the last week of follow-up (*C*) was also associated with a significant increase in bradycardia-related premature ventricular complexes (*D*). *$P < 0.05$; **$P < 0.01$ (*SI Appendix, SI Materials and Methods*).

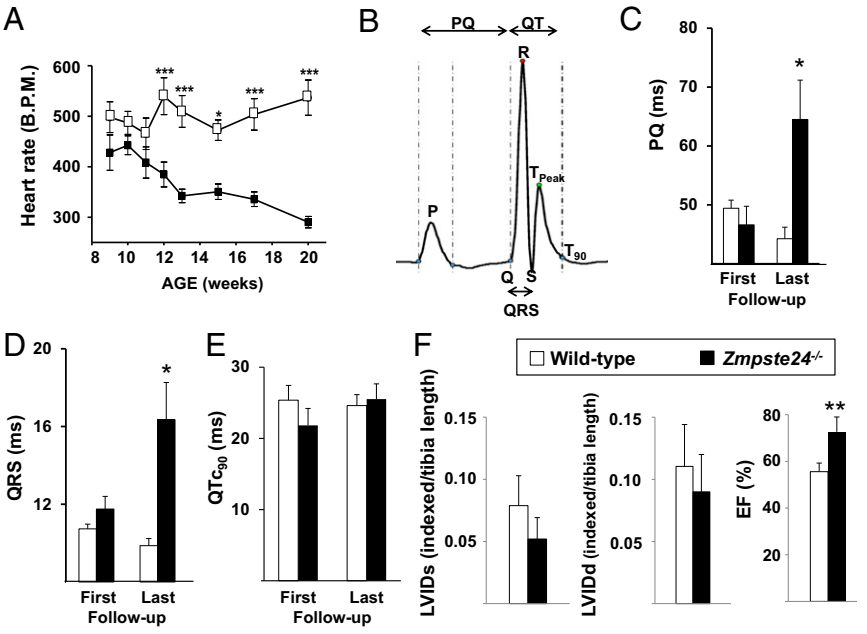

Fig. 3. *Zmpste24*$^{-/-}$ mice show preserved cardiac function but develop severe bradycardia and cardiac conduction abnormalities. (*A*) Heart rate (bpm) in conscious mice. (*B*) Template ECG showing the intervals used to quantify (*C*) PQ, (*D*) QRS, and (*E*) heart rate-corrected QT at 90% of repolarization from T_{peak} (QTc_{90}) duration measured on the baseline ECG at the first follow-up (week 11; First) and the last follow-up (Last) (*SI Appendix, SI Materials and Methods*). (*F*) LVIDs, LVIDd, and EF determined by transthoracic echocardiography in 18- to 20-wk-old mice. **P* < 0.05; ***P* < 0.01; ****P* < 0.001.

During both isoproterenol challenge (*SI Appendix*, Fig. S4) and recovery (*SI Appendix*, Fig. S5), *Zmpste24*$^{-/-}$ mice showed increased prolongation of PQ and QRS intervals. Progeroid *Zmpste24*$^{-/-}$ mice also developed age-dependent bradycardia in the absence of isoproterenol (Fig. 3*A*). In addition, at 18–20 wk of age, *Zmpste24*$^{-/-}$ mice showed significant signs of defective cardiac conduction compared with age-matched controls manifested as prolonged PQ interval and QRS complex, without alterations to the QTc interval (Fig. 3 *B*–*E* and *SI Appendix*, Table S3).

Preserved Cardiac Function in *Zmpste24*$^{-/-}$ Mice. Transthoracic echocardiography revealed no abnormalities in left ventricle end diastolic [left ventricular internal diameter at diastole (LVIDd)] or left ventricle end systolic [left ventricular internal diameter at systole (LVIDs)] parameters in progeroid *Zmpste24*$^{-/-}$ mice (Fig. 3*F*). Likewise, *Zmpste24*$^{-/-}$ mice had normal left ventricle mass, posterior wall and interventricular septal thickness at diastole (*SI Appendix*, Fig. S6*A*), and diastolic function but had a slightly higher left ventricle ejection fraction (EF) and fractional shortening than controls (Fig. 3*F* and *SI Appendix*, Fig. S6*A*), although within the normal range. The higher EF in progeriod mice might be explained by bradycardia, because longer diastolic intervals may favor such an increase. In fact, together, bradycardia and smaller body surface area in *Zmpste24*$^{-/-}$ mice explain the significantly lower cardiac output compared with WT controls (*SI Appendix*, Fig. S6*B*). However, cardiac index, which relates the cardiac output of the left ventricle per minute to body surface area, was not different between progeroid and WT mice (*SI Appendix*, Fig. S6*B*). Time course studies showed no between-genotype differences in systolic or diastolic blood pressure (*SI Appendix*, Fig. S6*C*).

Ex Vivo Cellular Electrophysiology. We next conducted electrophysiology studies in cardiac multicellular preparations from *Zmpste24*$^{-/-}$ mice to identify potential mechanisms underlying the arrhythmia risk associated with abnormal repolarization. No significant between-genotype differences were found in resting membrane potential, action potential (AP) amplitude, maximum velocity of depolarization (V_{max}), or AP duration in right or left ventricular samples (*SI Appendix*, Table S4). Moreover, APs recorded in right and left ventricular preparations were indistinguishable between genotypes (Fig. 4*A*). Interestingly, most *Zmpste24*$^{-/-}$ ventricular preparations exhibited slow spontaneous automatic activity at ~3 Hz (Fig. 4*B*). Also, *Zmpste24*$^{-/-}$ left ventricle preparations displayed afterdepolarizations that led to triggered APs, contrasting with normal AP in controls (Fig. 4 *B* and *C*).

We next analyzed transcription of genes encoding ion channel proteins involved in the different phases of the AP. Real-time quantitative PCR (qPCR) analysis in *Zmpste24*$^{-/-}$ hearts revealed no significant between-group differences in mRNA expression of *Scn5A* (encoding the cardiac sodium channel $Na_V1.5$; involved in cell depolarization) or *Kcna5*, *Kcnj2*, *Kcnd3*, and *Kcnq1* (encoding the potassium channels $K_v1.5$, Kir2.1, Kv4.3, and Kv7.1, respectively; all involved in AP repolarization); in contrast, *Zmpste24*$^{-/-}$ hearts showed significant up-regulation of *Kcnh2* (encoding the potassium channel Kv11.1, also known as human ether-à-go-go related gene (hERG; involved in AP repolarization) (*SI Appendix*, Fig. S7).

***Zmpste24*$^{-/-}$ Mice Show Defective Sarcoplasmic Reticulum Ca^{2+} Handling.** We next investigated the role of intracellular Ca^{2+} handling in the observed in vivo afterdepolarizations and triggered APs in multicellular left ventricle *Zmpste24*$^{-/-}$ preparations. Unlike WT cardiomyocytes, *Zmpste24*$^{-/-}$ cardiomyocytes were unable to maintain stable Ca^{2+} transients at higher stimulation frequencies, an effect that was more prominent at 5 mM extracellular Ca^{2+} (Fig. 5*A*). To test whether this defect in *Zmpste24*$^{-/-}$ cardiomyocytes was caused by unstable calcium release from the sarcoplasmic reticulum (SR) through the ryanodine receptor type 2 (RyR2) channel, we measured the frequency of spontaneous calcium waves at rest. However, we found no differences in the calcium wave frequency at any of the calcium concentrations examined (Fig. 5*B*). In line with these results, *Zmpste24* deficiency did not affect the transcript level of RyR2 (Fig. 5*C*), which is responsible for calcium release from the SR (12).

These findings suggested possible impairment of L-type Ca^{2+} currents (I_{Ca}) or Ca^{2+} uptake by the SR in *Zmpste24*$^{-/-}$ cardiomyocytes as alternative causes for unstable calcium transients. Compared with WT controls, *Zmpste24*$^{-/-}$ hearts expressed significantly lower transcript and protein levels of SR Ca^{2+} ATPase, whereas there was no alteration in transcript levels of *STIM1* (stromal interaction molecule component of the store-operated Ca^{2+} entry 1) and *Orai1* (component of the store-operated Ca^{2+} entry), essential regulators of Ca^{2+} release-activated Ca^{2+} channels (Fig. 5 *C* and *D*). We also analyzed the expression of

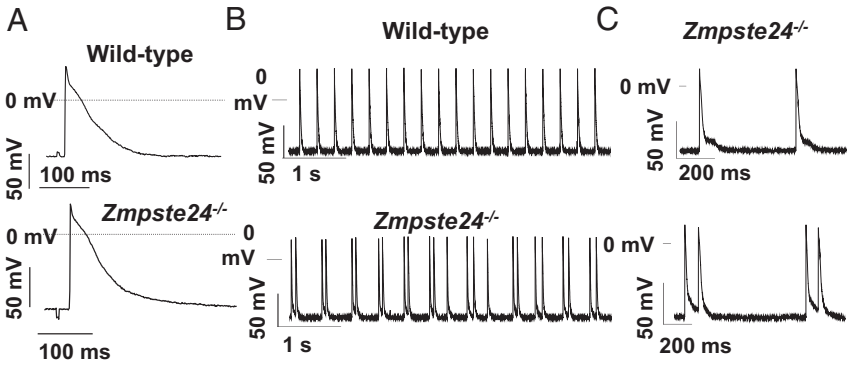

Fig. 4. Transmembrane APs recorded in multicellular left ventricular preparations. (*A*) Representative APs (3 Hz) from WT and *Zmpste24*$^{-/-}$ mice. (*B*) Left ventricular preparations from *Zmpste24*$^{-/-}$ mice displayed afterdepolarizations that occasionally yielded triggered APs (*C*, *Lower*).

calsequestrin 1 (*CSQ1*) and *CSQ2*, calcium-binding proteins of the SR that help this organelle store a very high amount of Ca^{2+} during relaxation in each contraction–relaxation cycle. Although *CSQ1* and *CSQ2* transcript levels were significantly lower in *Zmpste24*$^{-/-}$ hearts (Fig. 5*C*), no between-genotype differences were observed at the protein level (Fig. 5*D*). Likewise, peak I_{Ca} did not differ significantly between cardiomyocytes of the two genotypes (*SI Appendix*, Fig. S8).

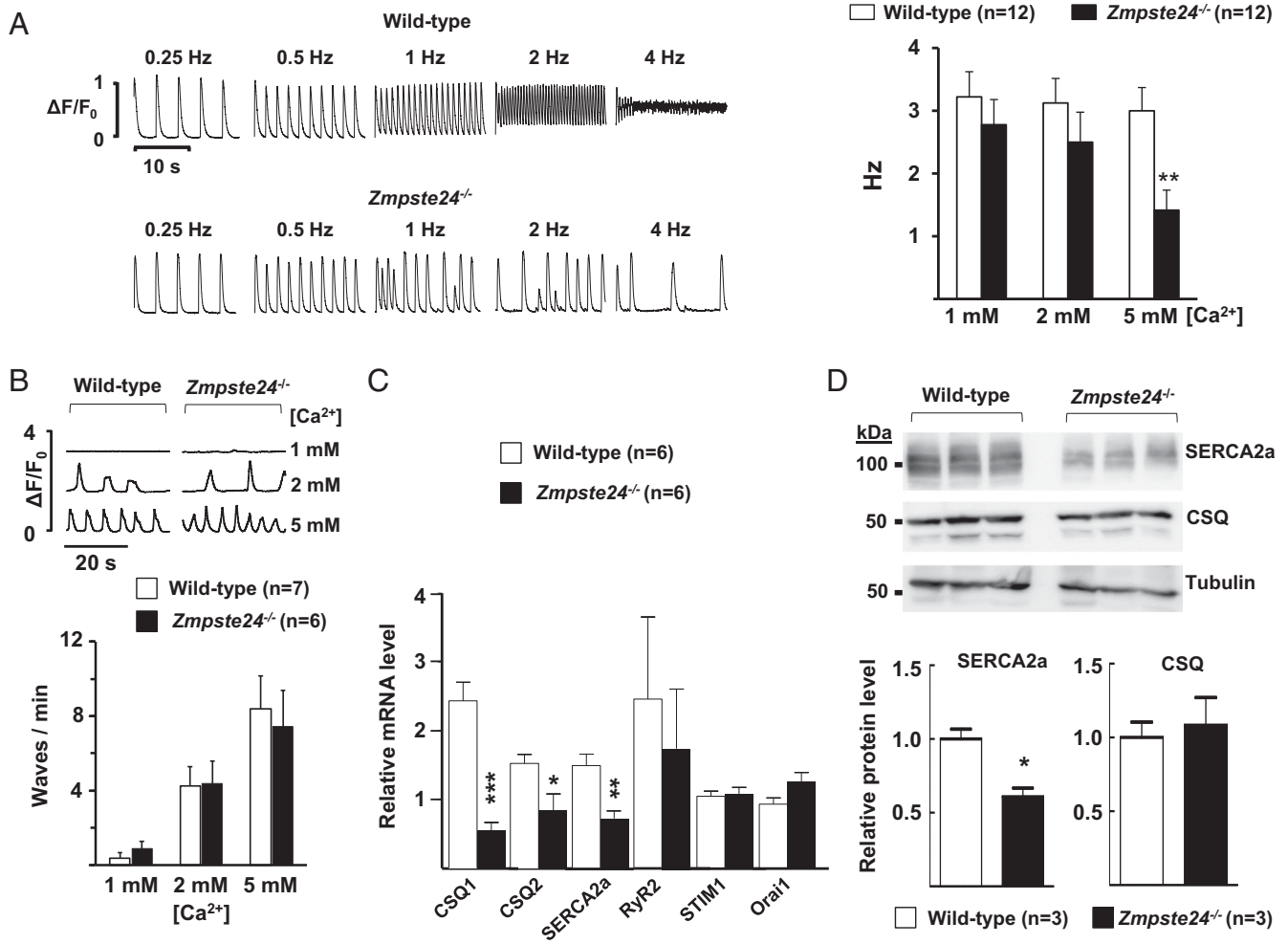

Fig. 5. Defective Ca^{2+} transients in *Zmpste24*$^{-/-}$ cardiomyocytes. (*A*, *Left*) Analysis of beat to beat response stability in isolated mouse ventricular myocytes subjected to increasing stimulation frequencies. Representative examples of calcium transients recorded in the presence of 5 mM extracellular $Ca^{2+}$are shown. Irregular beat to beat responses start at lower frequencies in *Zmpste24*$^{-/-}$ cardiomyocytes. (*A*, *Right*) The graph shows threshold frequencies (in hertz) for the induction of nonuniform beat to beat responses at the indicated Ca^{2+} concentrations. Responses were recorded in myocytes isolated from WT and *Zmpste24*$^{-/-}$ mice (12 cells from six mice of each genotype). (*B*, *Upper*) Typical recordings of spontaneous calcium waves at the indicated Ca^{2+} concentrations. (*B*, *Lower*) Calcium dependency of the calcium wave frequency. Values are from seven WT mice ($n = 15$ cells) and six *Zmpste24*$^{-/-}$ mice ($n = 14$ cells). (*C*) qPCR of heart tissue. (*D*) Western blot analysis of heart tissue. Representative blots are shown, and relative band intensity was quantified as described in *SI Appendix, SI Materials and Methods*. $^{*}P < 0.05$; $^{**}P < 0.01$; $^{***}P < 0.001$.

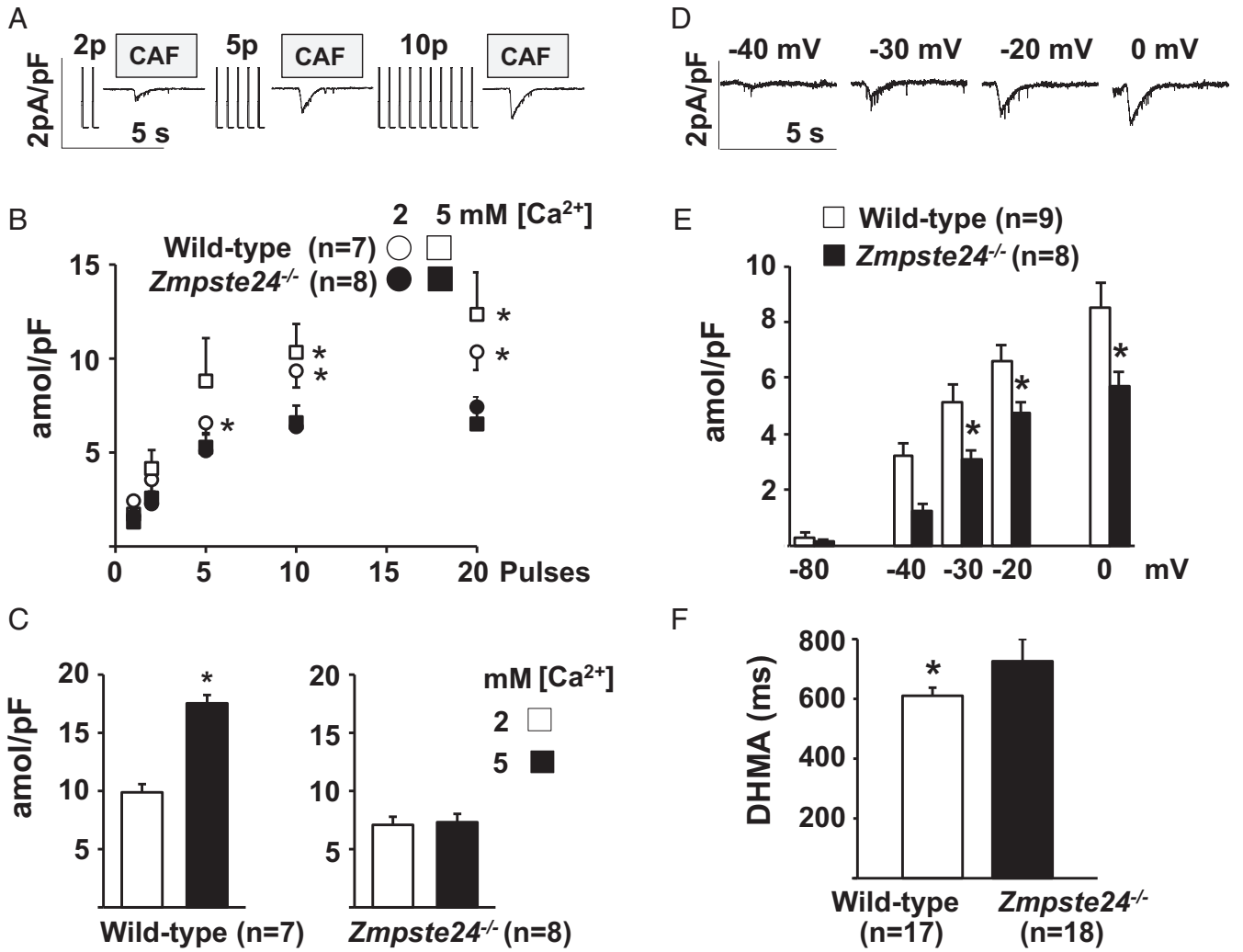

Fig. 6. Reduced maximal SR Ca^{2+} uptake in *Zmpste24*$^{-/-}$ cardiomyocytes. SR calcium loading capacity in isolated ventricular myocytes. (*A*–*C*) Calcium loading measured as a function of the number of stimulation pulses used for SR loading. (*A*) Representative caffeine (CAF)-induced currents recorded after SR reloading with the indicated number of stimulation pulses. Transient exposure to CAF was used to release SR calcium content before reloading and measure loading after the train of stimulation pulses. (*B*) Time integral of CAF-induced currents recorded after SR reloading with the indicated stimulation pulses. Data were obtained from seven *Zmpste24*$^{-/-}$ and eight WT myocytes (from $n = 5$ mice) exposed consecutively to 2 and 5 mM extracellular Ca^{2+}. Time integrals were converted to amoles and normalized to cellular capacitance (in picofarads). (*C*) Effect of extracellular calcium concentration on the time integral of CAF-induced current at steady state (after ≥30 stimulation pulses). (*D*–*F*) Calcium loading measured as a function of membrane potential. (*D*) Representative CAF-induced currents recorded after SR loading with a 5-s depolarization to the indicated membrane potentials. (*E*) Time integral of CAF-induced current recorded in the presence of 2 mM extracellular Ca^{2+} after SR reloading at rest (−80 mV) and after depolarizing to the indicated voltage. Data were obtained from eight *Zmpste24*$^{-/-}$ myocytes ($n = 5$ mice) and nine WT myocytes ($n = 6$ mice). (*F*) Mean calcium transient duration at half-maximal amplitude (DHMA) recorded in myocytes paced at 0.5 Hz (17 WT and 18 *Zmpste24*$^{-/-}$ myocytes from $n = 6$ mice per group). *$P < 0.05$.

To determine SR Ca^{2+} reloading function in ventricular cardiomyocytes, we loaded the SR by exposing cells to an increasing number of stimulation pulses and estimated the resulting Ca^{2+} load from caffeine-elicited inward current traces (Fig. 6*A*). SR reloading function was significantly weaker in *Zmpste24*$^{-/-}$ cardiomyocytes than in WT cells after 5, 10, and 20 stimulation pulses (Fig. 6*B*), and the defective response was still more apparent after ≥30 stimulation pulses (Fig. 6*C*). Significantly lower SR Ca^{2+} loading in *Zmpste24*$^{-/-}$ cardiomyocytes was also evident from caffeine-elicited current traces recorded after loading the SR by depolarizing the membrane potential for 5 s to −40, −30, −20, or 0 mV (Fig. 6 *D* and *E*). In addition, intracellular Ca^{2+} transients recorded in isolated cardiomyocytes paced at 0.5 Hz revealed a significantly longer Ca^{2+}-transient duration (at half-maximal amplitude) in *Zmpste24*$^{-/-}$ cells (Fig. 6*F*).

Finally, we measured the SR Ca^{2+} release-dependent inactivation of the I_{Ca} in response to consecutive stimulation pulses given after clearance of SR Ca^{2+} (Fig. 7*A*) to assess the feedback of SR calcium release on I_{Ca} inactivation. As expected, current traces recorded in WT cardiomyocytes showed a faster rate of I_{Ca} inactivation as the number of pulses used for SR reload increased from 1 (p1) to 30 (p30) (Fig. 7*B*). In contrast, the effect of SR loading on the I_{Ca} inactivation rate in *Zmpste24*$^{-/-}$ cardiomyocytes was very modest (Fig. 7*B*). Accordingly, the time constant for I_{Ca} inactivation decreased progressively with increasing pulse number in WT but not *Zmpste24*$^{-/-}$ cardiomyocytes (Fig. 7*C*). Moreover, the amplitude of the intracellular Ca^{2+} transient induced by repeated stimulation at 0.5 Hz was significantly lower in *Zmpste24*$^{-/-}$ cardiomyocytes (Fig. 7*D*). Together, these findings indicate that SR Ca^{2+} uptake and release are blunted in *Zmpste24*$^{-/-}$ cardiomyocytes, which also explains the failure of acute isoproterenol

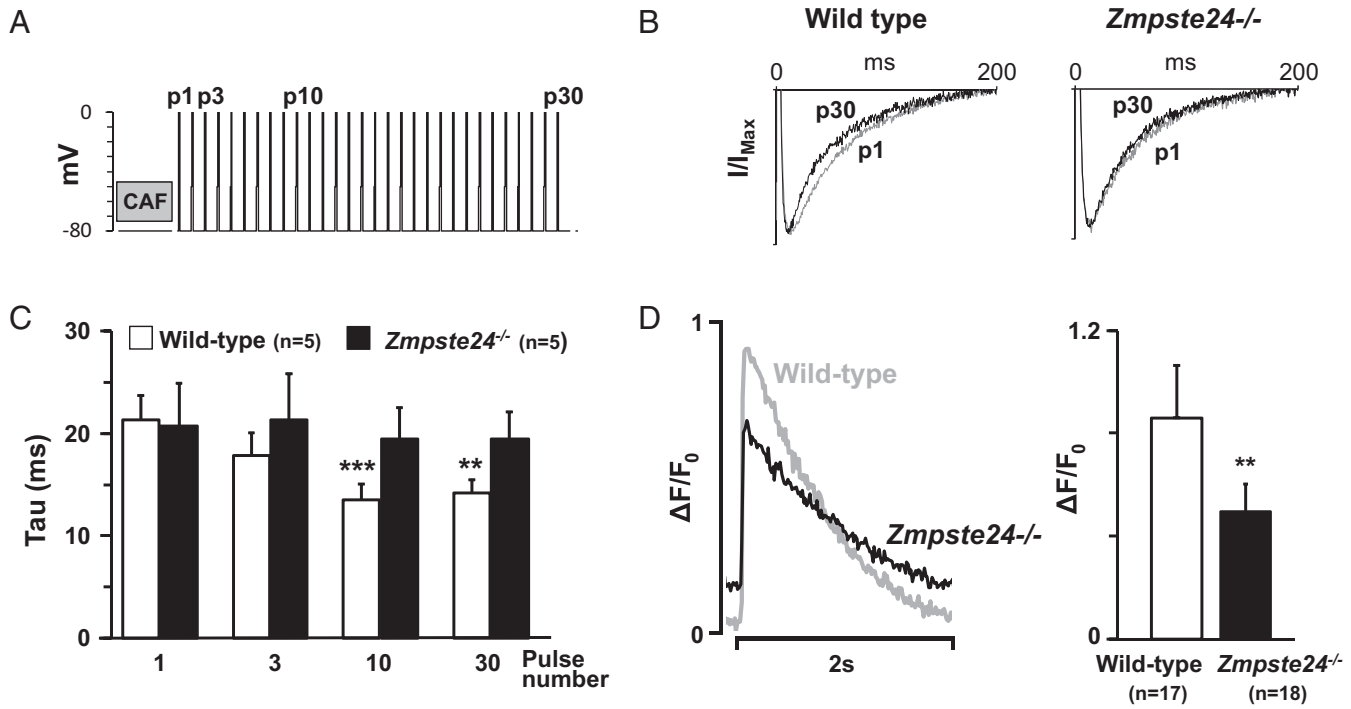

Fig. 7. Impaired SR calcium release-dependent inactivation of I_{Ca} in isolated *Zmpste24*$^{-/-}$ myocytes. (*A*) Protocol to measure the effect of SR calcium loading on I_{Ca} inactivation. SR calcium content was released with caffeine (CAF) and reloaded with a train of stimulation pulses. (*B*) Representative superimposed I_{Ca} recordings on p1 and p30. Currents were normalized to their peak values and fitted to a double-exponential equation. (*C*) Dependency of time constant (tau) for fast I_{Ca} inactivation on indicated pulses. (*D*) Representative calcium transient (ΔF/F0) recordings from myocytes paced at 0.5 Hz (*Left*) and calcium transient amplitude quantification (*Right*). Indicated cardiomyocytes are from $n = 6$ mice per genotype. $^{**}P < 0.01$; $^{***}P < 0.001$.

treatment to induce ventricular arrhythmia, despite abnormal repolarization.

Abnormal Connexin43 Localization in the Hearts of *Zmpste24*$^{-/-}$ Mice and HGPS Patients. To further investigate conduction alterations in progeria, we performed immunohistopathological studies in heart tissue. Cardiomyocyte size was estimated by quantifying their cross-sectional area in heart sections as well as the membrane capacitance, which is linearly proportional to the plasma membrane area and cell size. Because *Zmpste24*$^{-/-}$ mice are smaller than age-matched controls (9, 11), we normalized results by tibia length. Normalized cross-sectional area and membrane capacitance were similar in cardiomyocytes of both genotypes (*SI Appendix*, Fig. S9). We also performed Mallory's trichrome staining, which revealed normal chambers, ventricular walls, and myocardial fiber arrangement in *Zmpste24*$^{-/-}$ hearts (*SI Appendix*, Fig. S10 *A* and *B*). Moreover, Mallory's trichrome staining did not reveal increased fibrosis in the ventricular interstitium (*SI Appendix*, Fig. S10*B*) or key structures involved in cardiac conduction, such as the atrioventricular node and the main His bundles (*SI Appendix*, Fig. S10*C*), which might have explained conduction abnormalities in *Zmpste24*$^{-/-}$ mice. However, consistent with previous studies in HGPS patients (13), *Zmpste24*$^{-/-}$ mice showed extensive fibrosis in the tunica media of the major coronary arteries (*SI Appendix*, Fig. S11*A*) and discontinuous and weak expression of smooth muscle actin within the medial arterial layer (*SI Appendix*, Fig. S11*B*).

Another possible explanation for the observed cardiac conduction anomalies is altered expression of intercalated disk proteins that play a key role in intercellular connectivity, such as the gap junction protein connexin43 (Cx43) and plakoglobin, as well as cytoskeletal desmosome-interacting proteins, such as desmin, a class III intermediate filament connected to A-type lamins through Nesprin/Sun protein complexes. Western blot analysis in progeroid hearts revealed a significant approximately twofold increase in Cx43 expression without changes in plakoglobin or desmin (*SI Appendix*, Fig. S12). Remarkably, compared with WT controls, *Zmpste24*$^{-/-}$ cardiomyocytes exhibited marked mislocalization of Cx43 to the cytoplasm and the lateral long axis as revealed by double immunofluorescence to simultaneously detect Cx43 and N-Cadherin (Fig. 8*A*). Quantification of digital images revealed less Cx43/N-Cadherin colocalization in the hearts of progeroid mice than in WT controls (Fig. 8*E*).

Profound Cx43 mislocalization was also revealed by immunostaining of left ventricle specimens obtained from two HGPS patients at autopsy. In these patients, Cx43 was abundantly associated with the perinuclear rim (Fig. 8 *B–D*), which is its trafficking origin for subsequent targeting to the intercalated disks (14) (*Discussion*). Quantification of digital images confirmed a low percentage of Cx43/N-Cadherin colocalization in HGPS hearts (Fig. 8*E*). Defective cardiomyocyte connectivity associated to Cx43 mislocalization may contribute to cardiac conduction defects in progeria (*Discussion*).

Discussion

HGPS is a devastating genetic disease resulting from abnormal processing of prelamin A, which is characterized by premature cardiovascular disease and death at an average age of 14.6 y old (4). Here, we provide a comprehensive analysis of electrocardiographic abnormalities and underlying molecular changes at different stages of HGPS. Our findings may have implications for the risk of premature death in HGPS patients and potentially, normal aging, because defective prelamin A processing has also been revealed in cells and tissues of normally aging non-HGPS individuals (reviewed in refs. 2 and 7). A previous study identified repolarization abnormalities in 3 of 15 HGPS patients with the "classical" *LMNA* c.1824C > T mutation (3). Here, we confirm and extend these findings through a rigorous examination of a new

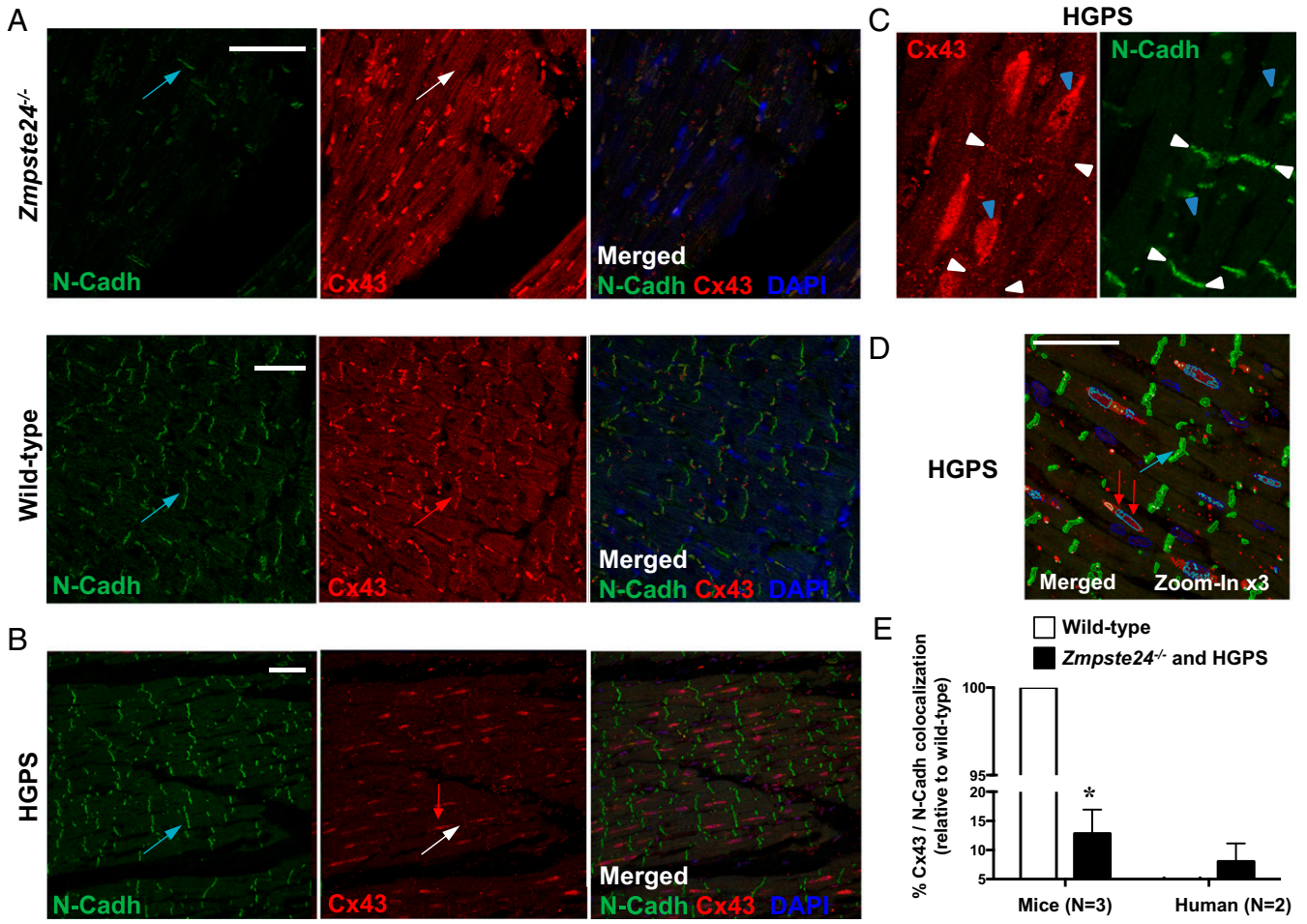

Fig. 8. Abnormal localization of Cx43 in hearts of progeroid *Zmpste24*$^{-/-}$ mice and HGPS patients. (*A* and *B*) Double immunofluorescence of left ventricle sections from mice of the indicated genotype and HGPS patients to detect N-Cadherin (N-Cadh; green in *Left*) and Cx43 (red in *Center*). *Right* shows merged images, with DAPI staining of nuclei (blue). (*A*) Cx43 lateralization was evident in *Zmpste24*$^{-/-}$ mice. Blue arrows mark examples of intercalated disk areas (N-Cadh positive). The white arrow in the *Zmpste24*$^{-/-}$ image marks an intercalated disk without Cx43 expression, and the red arrow in the WT image marks an intercalated disk with abundant Cx43 expression. (*B*) Representative images illustrating loss of Cx43/N-Cadh colocalization in HGPS heart. Blue arrow and white arrow are as in *A*. The red arrow marks a Cx43-positive area, which does not colocalize with N-Cadh. (*C*) Magnified view of an HGPS heart section. Blue arrowheads mark examples of predominant Cx43 expression near nuclei. White arrowheads mark examples of scant Cx43/N-Cadh colocalization at intercalated disks. (*D*) Automatic image segmentation of an HGPS heart section used for quantification of Cx43/N-Cadh colocalization. Green, red, and dark blue blob boundaries correspond to positive staining for N-Cadh, Cx43, and nuclei, respectively. Cyan blob boundaries represent areas showing Cx43/nuclei colocalization. (Scale bars: 50 μm.) (*E*) Percentage of Cx43/N-Cadh colocalization at the intercalated disks estimated by quantifying automatically segmented images. Results are represented relative to WT (=100); $n = 3$ WT and *Zmpste24*$^{-/-}$ mice and $n = 2$ HGPS patients were analyzed ($n = 5$ sections per individual). *$P < 0.001$.

cohort of 15 HGPS patients carrying the same mutation. One-half of the patients showed overt repolarization abnormalities in at least one ECG compatible with coronary artery disease (ST depression/elevation and negative and biphasic T waves). Repolarization abnormalities in HGPS patients were strongly evident at advanced disease stages. We also detected prominent mislocalization of Cx43 in left ventricle specimens obtained at autopsy from diseased HGPS patients; Cx43 mislocalization was also observed in the hearts of progeroid *Zmpste24*$^{-/-}$ mice and is indicative of defective cardiac conduction in progeria (see below).

Animal models resembling the clinical phenotype of HGPS patients are central to understanding the underlying mechanisms of the disease and developing novel therapies. Our analysis of the well-established *Zmpste24*$^{-/-}$ mouse model of progeria caused by prelamin A accumulation (9, 11) revealed the progressive development of cardiac rhythm alterations that can lead to premature death. *Zmpste24*$^{-/-}$ hearts and cardiomyocytes showed the following specific alterations: (*i*) T-wave repolarization abnormalities, which were also present in one-half of HGPS patients; (*ii*) prolonged PQ interval and wide QRS complex; (*iii*) development of bradycardia-related premature ventricular complexes and slow-rate polymorphic ventricular rhythms at late disease stages in the absence of ventricular arrhythmias during isoproterenol challenge; (*iv*) automatic spontaneous ventricular activity and afterdepolarizations ex vivo, which were associated with significantly slowed I_{Ca} inactivation and reduced amplitude of the intracellular Ca^{2+} transient; and (*v*) mislocalization of Cx43 in the heart.

Notably, some characteristics of the progeroid *Zmpste24*$^{-/-}$ mouse heart are also present in HGPS patients and frequently observed in normal aging; these characteristics include extensive fibrosis and loss of smooth muscle cells in coronary arteries, defective calcium homeostasis, progressive development of repolarization defects, and Cx43 mislocalization (15–17). Overt repolarization abnormalities in ST T waves and T-wave flattening in mice did not increase the risk of isoproterenol-triggered ventricular arrhythmia. However, T-wave alterations are well-known to increase the risk of lethal ventricular arrhythmias

during ischemia (18), which might contribute to premature death in HGPS patients from myocardial infarction, one of the main causes of death in this population. T-wave abnormalities might be explained at least in part by an altered repolarization pattern brought about by two opposing ion channel changes observed in the hearts of *Zmpste24*$^{-/-}$ mice: on the one hand, the significant up-regulation of *Kcnh2*, which encodes the hERG channel responsible for I_{Kr}, would help terminate the AP plateau and shorten repolarization (19), and on the other hand, the observed slow I_{Ca} inactivation would tend to prolong the plateau and delay repolarization (20). Importantly, an abnormally long QTc interval was observed in only 1 of 51 ECGs from 15 HGPS patients and occurred in the context of ischemia and significant repolarization anomalies. Consistently, we observed no significant QTc prolongation in *Zmpste24*$^{-/-}$ mice, in agreement with the normal AP duration observed in *Zmpste24*$^{-/-}$ ventricular cardiomyocytes and the majority of ECG traces from HGPS patients. Although we documented significant QRS complex widening in progeroid mice, it is important to note that the high-amplitude QRS complex in the mouse ECG represents not only the spread of depolarization across the ventricle but also, the early phase of repolarization (21). We, therefore, carefully examined QRS complex and QT duration (QT_{90}) (Fig. 3 *B*–*E*) to detect any significant increases in both parameters. However, mouse and human QT intervals must be compared with caution.

The occurrence of bradycardia-related premature ventricular complexes in *Zmpste24*$^{-/-}$ mice during recovery after isoproterenol shows a significant suppression of normal pacemaker activity, with emergence of ventricular ectopic escape discharges. Isoproterenol-induced heart rate increase in vivo is associated with increases in intracellular Na^+ and Ca^{2+} concentration (22); these changes, in the presence of the postisoproterenol-induced bradycardia, likely contributed to the escape discharges and premature ventricular complexes arising from the Purkinje system (*SI Appendix*, Fig. S3). Our ex vivo experiments with multicellular ventricular preparations showed afterdepolarizations during spontaneous ventricular activity at ∼3 Hz, which is similar to the cycle length after isoproterenol treatment in vivo. Although we were unable to establish the exact origin of these ventricular afterdepolarizations, the in vivo data support involvement of the Purkinje system, consistent with slow idioventricular discharges (cycle length = 266.38) (*SI Appendix*, Fig. S3) arising from varying Purkinje locations.

Connexins are the pore-forming subunits of gap junctions and essential for proper intercellular electrical coupling between cardiomyocytes and AP spread during each cardiac cycle (23, 24). Cx43 is the major connexin expressed in the ventricles. Its abnormal expression, typically involving down-regulation and heterogeneous redistribution to the lateral cardiomyocyte membrane, is associated with different forms of chronic heart disease (hypertrophic, dilated, and ischemic cardiomyopathy) and even aging (24–26). Defective Cx43 expression results in electrical defects in the myocardium and contributes to arrhythmogenesis. Therefore, Cx43 mislocalization in the heart may explain, at least partly, the prolongation of PQ interval and QRS complex in *Zmpste24*$^{-/-}$ mice. Interestingly, reduced gap junction coupling accompanied by Cx43 lateralization has been linked to reduced functional expression of the alpha subunit ($Na_V1.5$) of the cardiac sodium channel at the intercalated disk (27), and the reduced sodium current is likely to have contributed to the significantly impaired atrioventricular and intraventricular conduction in *Zmpste24*$^{-/-}$ mice. Previous computer simulations (28) suggest that, even in the presence of Cx43 mislocalization and low $Na_V1.5$ expression, a normal peak I_{Ca} with slow inactivation and reduced Ca^{2+} transients could maintain relatively safe conduction in the ventricles of *Zmpste24*$^{-/-}$ mice, albeit at a reduced velocity. However, a high intracellular Ca^{2+} concentration would have compromised propagation safety and caused earlier block as observed for reduced intercellular coupling (28). Because the intercalated disk is regarded as a functional unit, with gap junction formation requiring the presence of neighboring mechanical junctions (29), we tested the expression of desmin and plakophilin-2. However, our Western blot analysis in *Zmpste24*$^{-/-}$ hearts revealed no alterations in the expression of these proteins.

Consistent with the findings in *Zmpste24*$^{-/-}$ mice, immunofluorescence studies in left ventricle specimens from deceased HGPS patients revealed abnormal cellular distribution of Cx43 to a predominantly perinuclear localization. Because Cx43 is packaged into vesicles at the perinuclear trans-Golgi network and then transported to the intercalated disk (14), our findings suggest that abnormal prelamin A processing causes defective Cx43 targeting to its distinctive microdomain at the gap junctions. Additional *LMNA* mutations might also cause cardiomyopathy by altering connexin expression and/or cellular localization. For example, transgenic mice expressing the lamin A N195K mutant, which causes dilated cardiomyopathy with conduction system disease in humans, die at an early age because of arrhythmia, and such a phenotype correlates with cardiac Cx43 and Cx40 misexpression and/or mislocalization (30). Future studies are warranted to elucidate the mechanism causing defective Cx43 microdomain targeting to gap junctions and their contribution to abnormal cardiac conduction in progeria.

Some of the nuclear envelope alterations in the heart associated with prelamin A or progerin expression also occur during normal aging (15–17), suggesting that shared mechanisms might cause cardiac alterations in HGPS patients and the geriatric population. Consistent with this idea, prelamin A and progerin are both produced in the cells of normally aging individuals, thus raising the possibility that altered lamin A processing contributes to normal aging and associated cardiovascular disease (reviewed in refs. 2 and 7). Much like in normal human aging, progeroid *Zmpste24*$^{-/-}$ mice develop coronary fibrosis, bradycardia, and severe conduction abnormalities. Cardiac conduction abnormalities also arise during aging in WT mice and are associated with an increased incidence of arrhythmias (31). However, Ca^{2+} transients differ between *Zmpste24*$^{-/-}$ mice and normally aging WT mice (32), with *Zmpste24*$^{-/-}$ cardiomyocytes being unable to maintain stable Ca^{2+} transients at 4 Hz. Ventricular cardiomyocytes from aged WT mice also have a significantly higher incidence of spontaneous Ca^{2+} sparks than cells from young animals; however, we did not observe a similar difference between progeroid mice and age-matched controls. *Zmpste24*$^{-/-}$ mice show weakened I_{Ca} inactivation and defective SR Ca^{2+} uptake and release, features also observed in aging human atrial myocytes (15). In line with these findings, Ca^{2+} transient amplitudes are reduced in progeroid mice (Fig. 6), aged WT mice (32), and aged human atrial cardiomyocytes (15).

The progressively developing bradycardia and deteriorating cardiac conduction in progeriod mice also resemble clinical rhythm abnormalities observed in the elderly (16, 17). Although the most common age-related cardiac conduction abnormality in humans is degenerative fibrosis (33), *Zmpste24*$^{-/-}$ mice did not show abnormal fibrosis in the ventricular interstitium or the major conduction structures. However, in line with observations in HGPS patients (13), the coronary arteries of *Zmpste24*$^{-/-}$ mice showed extensive fibrosis and reduced accumulation of smooth muscle cells, potential causes of vascular stiffening, reduced coronary flow, and abnormal impulse generation in the sinoatrial node and conduction in the atria and ventricles. The latter may have also contributed to T-wave alterations, especially during isoproterenol challenge, as well as progressive development of bradycardia in progeroid *Zmpste24*$^{-/-}$ mice. In fact, human patients with coronary artery disease show a high prevalence of conduction abnormalities, such as atrioventricular or sinoatrial block (34).

We provide a comprehensive characterization of cardiac abnormalities in HGPS patients and progeroid *Zmpste24*$^{-/-}$ mice, identifying a number of cellular and molecular alterations in both species that are likely to contribute to defective cardiac repolarization and conduction in progeria. Future studies are warranted to establish direct causal connections between the presence of unprocessed prelamin A or progerin and the cardiac abnormalities associated with HGPS, with the goal of identifying novel targets for therapeutic intervention. Based on our findings, major efforts should be placed into elucidating the mechanisms causing Cx43 mislocalization in the heart of progeroid mice and HGPS patients. These studies may pave the way to developing efficient therapies to improve cardiac conduction in progeria.

Although ion channels are highly conserved between humans and mice, significant electrophysiological differences exist (35), making it difficult to translate mouse findings to the clinical arena. For example, although we observed a tendency toward a slower heart rate in older HGPS patients with longer follow-up, HGPS patients did not show the bradycardia and other conduction abnormalities that appeared progressively in *Zmpste24*$^{-/-}$ mice. This difference might be due to the lack of sequential ECG assessment in humans until very advanced disease stages. Indeed, human left ventricle specimens obtained by autopsy revealed reduced localization of Cx43 at gap junctions, consistent with altered ventricular conduction velocity.

Continuous telemetry and other invasive electrophysiological measurements would have been desirable in *Zmpste24*$^{-/-}$ mice. However, these animals show severe body weight loss (body weight of ∼9 g at late stages compared with ∼30 g in age-matched WT controls) and are physically extremely fragile, precluding the use of commercially available telemetry systems or any other invasive approaches to register specific arrhythmias forecasting premature death. The physical deterioration of HGPS patients also limits implementation of any invasive measurements (e.g., implantable loop recordings) to further study rhythm abnormalities.

Materials and Methods

Clinical information from children with HGPS was obtained from The Progeria Research Foundation Medical and Research Database (principal investigator L.B.G.) and approved by the Rhode Island Hospital and Brown University Institutional Review Boards (Providence, RI). All participants or parents provided written informed consent in the primary language of the participant or parent. When appropriate, interpreters were used for consenting. At least one ECG recorded no more than 3 y before death was obtained from each of 15 HGPS patients. Thirteen gender- and age-matched control volunteers were weighed, and ECG traces were recorded for comparison. All control volunteers or parents provided written informed consent. Animal studies were carried out in male *Zmpste24*$^{-/-}$ mice (11) and age-matched WT male littermates (all C57BL/6). Mice were reared and housed in accordance with institutional guidelines and regulations and all procedures with mice were approved by the Centro Nacional de Investigaciones Cardiovasculares Carlos III (CNIC) Ethical Committee. All other detailed materials and methods are described in *SI Appendix, SI Materials and Methods*.

ACKNOWLEDGMENTS. We thank María Jesús Andrés for technical assistance and help with art work, Susan Campbell for assistance with patient information, Maite Dubraska for assistance with blood sampling and ECG in control subjects, Inés Ortega and Virginia Zorita for animal maintenance and care, and Simon Bartlett for English editing. This work was supported by Spanish Ministry of Economy and Competitiveness (MINECO) Grants SAF2010-16044 and SAF2013-46663-R (to V.A.), SAF2011-30312 and SAF2014-58286-C2-1-R (to L.H.-M.), SAF2011-30088 (to E.D.), and SAF2014-52413-R (to C.L.-O.) and Fondo de Investigación Sanitaria del Instituto de Salud Carlos III Grants RD12/0042/0028 (to V.A.), RD12/0042/0011 (to J.T.), and RD12/0042/0002 (to L.H.-M.), with cofunding from the Fondo Europeo de Desarrollo Regional and the Progeria Research Foundation. J.A.G. is the recipient of a U-Mobility Grant from the Marie Curie cofunding of Regional, National and International Programme (Grant 246550). The Instituto Universitario de Oncología is supported by Obra Social Cajastur. The CNIC is supported by the MINECO and the Pro CNIC Foundation, and it is a Severo Ochoa Center of Excellence (MINECO Award SEV-2015-0505).

1. Andrés V, González JM (2009) Role of A-type lamins in signaling, transcription, and chromatin organization. *J Cell Biol* 187(7):945–957.
2. Trigueros-Motos L, González JM, Rivera J, Andrés V (2011) Hutchinson-Gilford progeria syndrome, cardiovascular disease and oxidative stress. *Front Biosci (Schol Ed)* 3:1285–1297.
3. Merideth MA, et al. (2008) Phenotype and course of Hutchinson-Gilford progeria syndrome. *N Engl J Med* 358(6):592–604.
4. Gordon LB, et al.; Progeria Clinical Trials Collaborative (2014) Impact of farnesylation inhibitors on survival in Hutchinson-Gilford progeria syndrome. *Circulation* 130(1):27–34.
5. Barrowman J, Wiley PA, Hudon-Miller SE, Hrycyna CA, Michaelis S (2012) Human ZMPSTE24 disease mutations: Residual proteolytic activity correlates with disease severity. *Hum Mol Genet* 21(18):4084–4093.
6. Osorio FG, et al. (2011) Cell autonomous and systemic factors in progeria development. *Biochem Soc Trans* 39(6):1710–1714.
7. Gordon LB, Rothman FG, López-Otín C, Misteli T (2014) Progeria: A paradigm for translational medicine. *Cell* 156(3):400–407.
8. Zhang H, Kieckhaefer JE, Cao K (2013) Mouse models of laminopathies. *Aging Cell* 12(1):2–10.
9. Varela I, et al. (2005) Accelerated ageing in mice deficient in Zmpste24 protease is linked to p53 signalling activation. *Nature* 437(7058):564–568.
10. Villa-Bellosta R, et al. (2013) Defective extracellular pyrophosphate metabolism promotes vascular calcification in a mouse model of Hutchinson-Gilford progeria syndrome that is ameliorated on pyrophosphate treatment. *Circulation* 127(24):2442–2451.
11. Pendás AM, et al. (2002) Defective prelamin A processing and muscular and adipocyte alterations in Zmpste24 metalloproteinase-deficient mice. *Nat Genet* 31(1):94–99.
12. Willis BC, et al. (2016) Constitutive intracellular Na+ excess in purkinje cells promotes arrhythmogenesis at lower levels of stress than ventricular myocytes from mice with catecholaminergic polymorphic ventricular tachycardia. *Circulation* 133(24):2348–2359.
13. Olive M, et al. (2010) Cardiovascular pathology in Hutchinson-Gilford progeria: Correlation with the vascular pathology of aging. *Arterioscler Thromb Vasc Biol* 30(11):2301–2309.
14. Smyth JW, et al. (2012) Actin cytoskeleton rest stops regulate anterograde traffic of connexin 43 vesicles to the plasma membrane. *Circ Res* 110(7):978–989.
15. Herraiz-Martínez A, et al. (2015) Ageing is associated with deterioration of calcium homeostasis in isolated human right atrial myocytes. *Cardiovasc Res* 106(1):76–86.
16. Jensen PN, et al. (2014) Incidence of and risk factors for sick sinus syndrome in the general population. *J Am Coll Cardiol* 64(6):531–538.
17. Strait JB, Lakatta EG (2012) Aging-associated cardiovascular changes and their relationship to heart failure. *Heart Fail Clin* 8(1):143–164.
18. Verrier RL, Ikeda T (2013) Ambulatory ECG-based T-wave alternans monitoring for risk assessment and guiding medical therapy: Mechanisms and clinical applications. *Prog Cardiovasc Dis* 56(2):172–185.
19. Perry M, Sanguinetti M, Mitcheson J (2010) Revealing the structural basis of action of hERG potassium channel activators and blockers. *J Physiol* 588(Pt 17):3157–3167.
20. Madhvani RV, et al. (2015) Targeting the late component of the cardiac L-type Ca2+ current to suppress early afterdepolarizations. *J Gen Physiol* 145(5):395–404.
21. Mitchell GF, Jeron A, Koren G (1998) Measurement of heart rate and Q-T interval in the conscious mouse. *Am J Physiol* 274(3 Pt 2):H747–H751.
22. Vassalle M (1977) The relationship among cardiac pacemakers. Overdrive suppression. *Circ Res* 41(3):269–277.
23. Vaidya D, et al. (2001) Null mutation of connexin43 causes slow propagation of ventricular activation in the late stages of mouse embryonic development. *Circ Res* 88(11):1196–1202.
24. Fontes MS, van Veen TA, de Bakker JM, van Rijen HV (2012) Functional consequences of abnormal Cx43 expression in the heart. *Biochim Biophys Acta* 1818(8):2020–2029.
25. Peters NS (1996) New insights into myocardial arrhythmogenesis: Distribution of gap-junctional coupling in normal, ischaemic and hypertrophied human hearts. *Clin Sci (Lond)* 90(6):447–452.
26. Saffitz JE, Schuessler RB, Yamada KA (1999) Mechanisms of remodeling of gap junction distributions and the development of anatomic substrates of arrhythmias. *Cardiovasc Res* 42(2):309–317.
27. Cerrone M, et al. (2012) Sodium current deficit and arrhythmogenesis in a murine model of plakophilin-2 haploinsufficiency. *Cardiovasc Res* 95(4):460–468.
28. Shaw RM, Rudy Y (1997) Ionic mechanisms of propagation in cardiac tissue. Roles of the sodium and L-type calcium currents during reduced excitability and decreased gap junction coupling. *Circ Res* 81(5):727–741.
29. Delmar M, McKenna WJ (2010) The cardiac desmosome and arrhythmogenic cardiomyopathies: From gene to disease. *Circ Res* 107(6):700–714.
30. Mounkes LC, Kozlov SV, Rottman JN, Stewart CL (2005) Expression of an LMNA-N195K variant of A-type lamins results in cardiac conduction defects and death in mice. *Hum Mol Genet* 14(15):2167–2180.
31. Signore S, et al. (2015) Late Na(+) current and protracted electrical recovery are critical determinants of the aging myopathy. *Nat Commun* 6:8803.
32. Howlett SE, Grandy SA, Ferrier GR (2006) Calcium spark properties in ventricular myocytes are altered in aged mice. *Am J Physiol Heart Circ Physiol* 290(4):H1566–H1574.
33. Ferrer MI (1982) The etiology and natural history of sinus node disorders. *Arch Intern Med* 142(2):371–372.
34. Hsueh CW, Lee WL, Chen YT, Ting CT (2001) The incidence of coronary artery disease in patients with symptomatic bradyarrhythmias. *Jpn Heart J* 42(4):417–423.
35. London B (2001) Cardiac arrhythmias: From (transgenic) mice to men. *J Cardiovasc Electrophysiol* 12(9):1089–1091.

SUPPORTING INFORMATION APPENDIX

Cardiac electrical defects in progeroid mice and Hutchinson-Gilford progeria syndrome patients with nuclear lamina alterations

José Rivera-Torres, Conrado J. Calvo, Anna Llach, Gabriela Guzmán-Martínez, Ricardo Caballero, Cristina González-Gómez, Luis J. Jiménez-Borreguero, Juan A. Guadix, Fernando G. Osorio, Carlos López-Otín, Adela Herraiz-Martínez, Nuria Cabello, Alex Vallmitjana, Raul Benítez, Leslie B. Gordon, José Jalife, José Mª Pérez-Pomares, Juan Tamargo, Eva Delpón, Leif Hove-Madsen, David Filgueiras-Rama, Vicente Andrés

GLOSSARY OF ELECTROCARDIOGRAPHIC PARAMETERS

Bradycardia (in mice): A heart rate slower than normal average values in mice using the same protocol for anesthesia. Average heart rate in mice anesthetized with isoflurane (like in the present studies) has been previously reported at 450±17 bpm (1, 2), therefore bradycardia in our studies is considered at heart rates below such values.

Bradycardia (in children >3 years of age): A heart rate <60 bpm.

P wave: First positive deflection observed in the ECG, representing atrial depolarization.

PQ interval: Time between the beginning of atrial depolarization and the beginning of ventricular depolarization.

PR interval: Time from the onset of the P wave to the start of the QRS complex; it mainly reflects conduction through the AV node.

Q wave: Any negative deflection that precedes an R wave.

QRS: Series of deflections in an electrocardiogram that represent electrical activity generated by ventricular depolarization.

QT interval: Time from the start of the Q wave to the end of the T wave.

QTc: Duration of the QT interval corrected for the patient's heart rate.

R wave: The initial upward deflection of the QRS complex, after the Q wave; it represents ventricular depolarization.

RR interval: Time between two consecutive R waves in the electrocardiogram; it represents a complete cardiac cycle (patient's heart rate).

ST segment: The flat, isoelectric section of the ECG between the end of the S wave and the beginning of the T wave.

T wave: Electrocardiogram deflection that represents the electrical activity produced by ventricular repolarization.

SI MATERIALS AND METHODS

Electrocardiographic analysis of human ECG. Standard ECG recordings from human age-matched controls volunteers and HGPS patients were used to assess differences in repolarization abnormalities. Lead II and precordial V5 traces, commonly used for diagnosis of repolarization abnormalities (3) were selected to assess temporal and morphological differences between controls and patients, at the initial follow-up and advanced stages of the disease (last follow-up).

A semi-automatic approach was used for digitization using a Matlab-based custom tool **(Supplemental Figure S13)**, as previously described (4). Briefly, ECG recordings were scanned to a digital image (600 dpi) and stored in a codified digital format. To identify ECG traces on the standard ECG-paper, image-processing techniques were applied involving binary thresholding, pixel-to-point conversion and transform techniques. When necessary, images were pre-processed to avoid artifacts (contrast, median filtering and interpolation) in the digitization process. Pixel-to-point conversion was applied using the lower waveform envelope. The graphical grid was used as reference for interpretation.

Corrected QT interval (QTc) was calculated using Bazett's formula, and considered prolonged when >450 ms for men and >470 ms for women (5). Age-dependent effects on human repolarization variability were quantified from averaged ECGs extracted from standard paper-ECG lead II **(Supplemental Fig.S13).** Human repolarization alterations were quantified using a rate-independent T-wave flattening score obtained from averaged area-normalized T-waves and compared with age-matched controls **(Supplemental Fig.S13)** (6). The human T-wave Flattening Score was compared with ECG traces from age-matched healthy controls. The formulation applied is described below:

$$Human\,T_{wave}\,Flattening\,Score = \left(1 - \frac{\sqrt[4]{M_4}}{0.1 \cdot M_2^2}\right)$$

$$where:$$

$$M_k = \frac{\left[\sum_{i=1}^{n} (x_i - \bar{x})^k \cdot T(i)\right]^{\frac{1}{k}}}{Var\_T^2};$$

where T wave flatness is obtained for the unit area normalized T-wave. We used a modified and corrected peakedness factor described by the 4^{th} central moment normalized to the variance. The score was corrected to allow increasing values of flatness reflect increasing values of flattening of the T-wave.

All data analyses, extraction and quantifications were done using custom scripts written in MATLAB software (version 8.1 release R2013a, The MathWorks Inc, Natick, Massachusetts, USA).

Beat-to-beat variability of the RR interval series was primarily assessed using 2-dimensional representations of the pairs RR_n-RR_{n+1} (n=cardiac beat number within the entire registration period) color-coded for time from blue to red.

Time-course electrocardiographic analysis of mouse cardiac rhythm abnormalities. Mice were anesthetized with 1.5-2% isoflurane in oxygen, inhaled through a facial mask. To avoid night-day circadian variations, ECG was performed in the morning. ECG electrodes were inserted subcutaneously in the four limbs and sequential ECG recordings were acquired at 2 KHz sweep-speed using a MP36R data acquisition workstation (Biopac Systems). Data were stored for off-line analysis using custom

MatLab scripts. From 11 weeks of age (First week) until 19 weeks of age or death of the animal (Last week), *Zmpste24*$^{-/-}$ and wild-type mice were given weekly β-adrenergic challenge with isoproterenol (i.v. bolus 0.34 mg/kg). ECG traces were recorded at baseline, after challenge, and during recovery (10 to 25 min).

ECG recordings were analyzed offline using custom scripts for pre-processing, visualization and quantification of electrophysiological intervals and heart rate variability markers. After band-pass filtering between 0.5-250 Hz, baseline wander was removed using a bidirectional filtering strategy. Baseline drift removal is essential for morphological analysis of T-waves. **Supplemental Figure S4** shows averaged ECG from WT and *Zmpste24*$^{-/-}$ mice obtained after Q-wave alignment from up to 100 beats in mice at baseline, prior to β-adrenergic stimulation. Specifically: i) PR intervals were measured from the beginning or the P wave to the peak of the R wave; ii) QRS intervals were measured from the beginning of the Q wave until the point where the S wave crosses the baseline; and iii) QT intervals were measured from the beginning of the Q wave until the point where the T-wave declines to 90% (T_{90}) from the peak (7). Finite differential methods and wavelet transform were used for fiducial point estimation. R-peak detection was robustly estimated by parabolic fitting of the coiflet wavelet transform and detection of the maximum magnitude point. All R detections were supervised to ensure accuracy of ECG segmentations. After QRS detection, P and T wave segments were extracted using adaptive windowing depending upon beat-to-beat RR changes. After segmentation using differential methods, both waves were low-pass filtered at 20 Hz using a Kaiser window FIR filter.

Adaptive heart-rate-corrected QT values (QTc) were derived using a modification of Bazzet's formula for murine electrocardiography (8). RR and QTc dispersion were assessed as the difference between the maximum and minimum intervals measured. Up to 5 minutes of recordings, aligned to the Q-wave, were used to obtain signal-averaged ECG (SAECG) traces, where additional electrophysiological parameters were quantified for data analyses. Quantified variables were mean P-wave duration, QRS duration, T-wave duration and dispersion, Q-wave to T_{peak}, and T_{peak} to T_{90} (90% of repolarization from T_{peak}) (not shown). All measured intervals were based on previous studies in murine electrophysiology (9).

T-wave morphological alterations were quantified by defining a modified flattening kurtosis-based descriptor derived for mice (6) **(Supplemental Figure S14).** T-wave SAECG in each segment of interest (up to 5 minutes, 2143±274 complexes) was considered for T-wave parameterization. SAECG traces were appropriately de-trended and rectified to determine the T-wave onsets. T-wave offset was determined as the 90% repolarization from the T-wave peak (T_{90}). T-wave end (T_{end}) was defined as the maximum change in slope during recovery to the isoelectric line. T-waves were interpreted as unit-area normalized probability density functions (TPDFs) for kurtosis estimation to describe the peakedness of the distribution as compared to a Gaussian distribution function. The flattening score was defined as the product of a geometric factor multiplied by the inverted normalized kurtosis corrected to achieve increasing values of flattening score with increasing flatness of the T-wave. The equation applied is:

$$Mice\,T_{Wave}\,Flattening\,Score = 0.25 \cdot \left[\frac{(1 - \frac{\sqrt[4]{M_4}}{M_2^2}) \cdot (1 - \left[\frac{T_d}{T_p - T_{on}} \right]^{\frac{1}{2}})}{1 + dTdt_{\max} \cdot A_T^2} \right]^{\frac{1}{4}}$$

where the peakedness factor is described by the central moments used to obtain excess kurtosis (fourth central moment normalized to the squared second moment) of the TPDFs were calculated as described elsewhere (10). A geometrical correction factor includes T_d and T_p-T_o as the averaged T-wave duration and the T elevation from the isoelectric line. A_T represents the area prior to normalization and $dTdt_{max}$ the T-wave upstroke depolarization. **Supplemental Figure S14** shows representative traces of SAECGs with corresponding segmented T-waves and flattening score values for *Zmpste24*$^{-/-}$ and wild-type mice in each segment of interest for the initial (First; 11 week) and last week of follow-up.

All the above-described ECG measures were quantified in *Zmpste24*$^{-/-}$ mice and controls at baseline (1 minute), after ß-adrenergic stimulation to exacerbate the *Zmpste24*$^{-/-}$ phenotype (5 minutes), and during recovery (4 minutes). Any premature ventricular complexes (PVC) or spontaneous ventricular rhythms were quantified and classified as isoproterenol-related or bradycardia-related.

Heart rate variability analysis in mice. We quantified short and mid-term heart rate variability (HRV) markers from ECG recordings of up to 25 min. Time domain, frequency domain geometrical and non-linear standard HRV descriptors (11) were automatically quantified using custom scripts in Matlab. All R-waves detected were considered for the offline heart rate variability analysis. A mean of 5739±1402 complexes was considered in each animal. Time domain descriptors included the mean and standard deviation of the RR interval series, as well as descriptors for quantification of beat-to-beat rate differences.

Mouse transthoracic echocardiography. Two-dimensional and M-mode echocardiography studies were performed weekly in anesthetized mice (1.5-2% isoflurane in a mixture with oxygen by a facial mask) using a Vevo 770 system (VisualSonic) equipped with a 30-MHz linear transducer probe. To avoid night-day circadian variations, echocardiography was performed in the morning. Before echocardiography, animal fur was removed with a topical depilatory agent and animals were warmed to maintain body temperature. The heart was imaged in the 2D parasternal long- and short-axis projections with guided M-mode recordings at the midventricular level in both views. LV end-diastolic diameter (LVEDD), LV-systolic diameter (LVESD), end-diastolic LV anterior wall thickness (LVAW), and LV posterior wall thickness (LVPW) were measured from images obtained by M-mode echocardiography. LV fractional shortening (FS) was calculated as follows:

$$FS\ (\%) = [(LVEDD-LVESD)/LVEDD][100].$$

LV ejection fraction (EF) and LV mass were calculated as follows:

$$EF\ (\%) = [(LVEDD3-LVESD^3)/LVEDD^3][100]$$

$$LV\ mass\ (mg) = [1.053][(LVEDD + LVAW + LVPW)^3 - (LVEDD)^3]$$

Blood pressure measurements in mice. A noninvasive automated tail-cuff device was used (Visitech System BP2000, NC). Mice were trained on a daily basis for one week, and weekly measurements were made at the same time in the morning. For greater accuracy, the first 10 of 20 measurements were discarded, and mean of the last 10 measurements were used for analysis.

Histomorphologic characterization of mouse heart. *Zmpste24*$^{-/-}$ and wild-type hearts were fixed in 4% paraformaldehyde, embedded in paraffin, sectioned with a microtome (10μm) and mounted on poly-L-lysine-coated glass slides. Routine histological analysis was performed using picrosirius red and Mallory's trichrome staining.

Coronary artery fibrosis was quantified in Mallory's trichrome-stained sections from 5 animals of each genotype. Large caliber arteries at the interventricular septum and free ventricular walls were identified and 3 transverse arterial profiles photographed along a total length of 300-400 μm (a minimal distance of 30 μm between sections was observed). Fibrosis was plotted against the total surface of the arterial medial wall using Adobe Photoshop, and the percentage of fibrotic pixels with respect to the total arterial surface was calculated with FiJi software. Statistical significance was assessed using t-Student's test by separately comparing each mutant specimen with a matched control, as well as by comparing pooled data from all mutants and wild-type specimens.

To quantify cardiomyocyte size, Mallory's-trichrome-stained left and right ventricular sections from 4 mice of each genotype were photographed with a NIKON DXM1200 camera. The profiles of individual cardiomyocytes were manually defined using Adobe Photoshop. The total area of each cardiomyocyte cross section (as an estimate of cell diameter/minor axis) was plotted as a black domain on a white background. Ninety cardiomyocytes were analyzed per ventricle (right/left) and specimen. NIH ImageJ software was used to quantify the total number of pixels per discrete black area (cardiomyocyte surface) in mice of both genotypes.

Autopsy specimens. Paraffin-embedded autopsy left ventricle specimens from HGPS patients HG028 and HG120 were obtained from the Cell and Tissue Bank of the Progeria Research Foundation (Rhode Island Hospital, Providence, RI) (www.progeriaresearch.org/cell_tissue_bank.html). Tissues were fixed in 2% paraformaldehyde and embedded in paraffin. Mutational analysis via the PRF Diagnostics Program (www.progeriaresearch.org/diagnostic_testing.html) identified the *LMNA* c.1824C>T mutation in both patients.

Immunohistochemistry. Mouse heart sections were immunostained using primary antibodies against smooth muscle α-actin (SMα-actin; SIGMA). Sections were dewaxed and rinsed with PBS. Endogenous peroxidase was quenched with 6% H_2O_2 and specimens were blocked in 1% BSA + 5% goat serum + 0.1% Triton X-100 for 3 h at room temperature. Slides were then incubated with primary antibody diluted in PBS (overnight, 4ºC), washed in PBS, and incubated with biotinylated anti-mouse smooth muscle α-actin for 3 h at room temperature. After washing in PBS, the samples were incubated in HRP-conjugated ExtrAvidin (SIGMA), and peroxidase activity was developed using the SIGMA Fast kit (Urea buffer + DAB). After final washes in water, specimens were dehydrated and mounted in DePeX (VWR BDH) for light microscopy inspection.

Double immunostaining for connexin 43 (Cx43) and N-cadherin (N-Cadh) was performed in left ventricular transverse-sections (10μm) from mice and HGPS patients HG028 and HG120 (see above "Autopsy specimens"). Antigens were retrieved by heating in TEG buffer (25 mM Tris-HCl pH 8, 10 mM EDTA 50 mM glucose) in a pressure cooker. Before primary IgG incubation, endogenous biotin was blocked using an avidin/biotin blocking kit (Vector Laboratories). Non-specific IgG binding was blocked with SBT solution (5% goat serum, 1% BSA and 0.5% Triton X-100 in Tris-PBS). Samples were incubated overnight (4ºC) with anti-Cx43 (1:50 in SBT, ABNOVA Anti-GJA1) and anti-NCadh (1:50 in SBT, DSHB-MNCD2). After extensive washes with PBS, sections were incubated for 2 h with biotinylated anti-rabbit IgG (1:100 in PBS), washed again in PBS, and incubated in TRITC-coupled extravidin and anti-mouse FITC for 2 h at room temperature. After final PBS washes, cell nuclei were counterstained with DAPI (1:2000 in PBS) and slides were mounted in Glicerol/PBS (1:1). Samples were visualized with a SP5 laser confocal microscope (LEICA).

Quantification of Cx43 mislocalization in heart sections. Image analysis of raw inmunohistochemical fluorescently-labeled mouse and human heart sections was performed to accurately quantify Cx43 localization at the intercalated disks. Extracted hyperstacks were separated into independent channels prior to image pre-processing. Two-dimensional median filtering with a

5x5 neighborhood was applied to minimize salt-and-pepper background noise. Semi-automatic segmentation by multidimensional histogram thresholding based on pixel intensities was applied to obtain binary feature extracted images and was corrected if necessary to optimize levels within each channel across heart sections. Additional morphological operations were applied for each individual binary mask, including filling, erosion and dilatation with a disk-shaped structuring element of radius = 4 pixels neighborhood to remove false positives. Detected blobs were delineated using a connectivity kernel of 8 pixels and used for binary image operations to determine staining and determine % co-localization among staining channels. A circularity score was defined as previously validated using ImageJ software (12). Cx43 was considered to be accumulated laterally when not co-localizing with the intercalated disks (N-Cadh) or internalized near the nuclei (co-localizing with DAPI), which simultaneously presented high (>0.5) circularity scores. All automatically segmented images were inspected by two independent investigators to validate the methodology.

Quantitative real-time PCR (qPCR). Total RNA was extracted from mouse heart apex tissue using QIAzol reagent (QIAGEN). cDNAs were synthesized using the SuperScript III First- Strand Synthesis System for RT-PCR (Invitrogen) and oligo dT primers. cDNA amounts were determined by qPCR using SYBR green qPCR Mix (Applied Biosystems). PCR conditions for amplification of all genes were 1 min at 95ºC and 40 cycles of 95ºC for 30 s, 57ºC for 30 s, and 72ºC for 30 s. Specificity of the SYBR green assays was confirmed by melting-point curve analysis. Expression data were calculated in qBASE from the cycle threshold (Ct) value using the ΔΔCt quantification method. Gene expression of 18S rRNA and GAPDH were used for normalization. Primers used for amplification are as follows:

GENE	Forward (5' – 3')	Reverse (5' – 3')
Orai1	AACGAGCACTCGATGCAGG	GGGTAGTCATGGTCTGTGTCC
STIM	TGACAGGGACTGTACTGAAGATG	TGCCGAGTCAAGAGAGGAGG
CSQ1	CTCATCAGCAGAAGGCAGGT	TTGACCTGTCAGCTCCACAA
CSQ2	TGCTCATGGTGGGGGTTTATC	AGGTTCGTGGTAATAGAGACAGA
SERCA2a	GAGAACGCTCACACAAAGACC	ACTGCTCAATCACAAGTTCCAG
RyR2	GCAGTCCCTGTCAGTACGG	CGTGTCCATAGAGGAGTGTCC
SCN5A	ATGGCAAACTTCCTGTTACCTC	CCACGGGCTTGTTTTTCAGC
KCND3	CCGGTCCCTGTGATAGTCTC	AGGGGATCATCCACAAGATAGG
KCNQ1	CGCGGTGGTCAAGAAGTGT	CACTGTAGATGGAGACCCG
KCNJ2	ATGGGCAGTGTGAGAACCAAC	TGGACTTTACTCTTGCCATTCC
KCNH2	GTGCTGCCTGAGTATAAGCTG	CCGAGTACGGTGTGAAGACT
KCNA5	TCCGACGGCTGGACTCAATAA	CAGATGGCCTTCTAGGCTGTG

Western blot. Mouse hearts were dissected, extensively washed with PBS and immediately snap-frozen in liquid nitrogen until further use. The hearts were ground with a mortar while frozen, further disrupted with TissueLyser (QIAGEN), and homogenized after incubation for 30 min at 4ºC with gentle rocking in lysis buffer (50 mM Tris-HCl pH 7.5; 0.1 M NaCl, 1 mM $MgCl_2$, 1 mM DTT, and 2% TX-100) supplemented with phosphatase and protease inhibitor cocktails (Roche). Protein concentration was determined by the Bradford assay (Protein Assay Kit, Bio-Rad). Cell extracts were preserved at -80ºC until use. For protein analyses, total protein extracts (40 µg) were mixed with Laemmli sample buffer (62.5 mMTris-HCl, pH 6.8, 2.3% SDS, 10% glycerol, 5% β-mercaptoethanol, 0.005% bromophenol blue), boiled for 10 min, and resolved on 10-12% SDS-polyacrylamide gels. Proteins were transferred to PVDF membranes using the iBlot Dry Blotting system (Invitrogen). Membranes were incubated for 1 h at room temperature in blocking buffer (5% non-fat dried milk in TBS, 0.2% Tween-20) followed by incubation with primary antibodies diluted in blocking buffer (overnight, 4ºC). Primary antibodies were purchased from Sigma-Aldrich (anti-

tubulin, ref. T9026), Invitrogen (anti-Cx43, ref. 71-0700), Abcam (anti-desmin, ref. ab8592; anti-CSQ, ref ab3516), Beckton Dickinson (anti-plakoglobin; ref BD610253), and Santa Cruz Biotechnology (anti-Serca2, ref sc8095). After washes with TBS, 0.2% Tween-20, membranes were incubated with appropriate HRP-conjugated secondary antibodies (Santa Cruz) for 1 h at room temperature, and specific proteins were visualized by enhanced chemiluminescence (GE Healthcare).

To quantify relative protein levels in heart, western blots were performed with heart extracts from 3 wild-type and 3 *Zmpste24*$^{-/-}$ mice. The intensity of protein bands was determined by densitometric analysis of independent blots for each lysate (2 blots for plakoglobin and SERCA2 and 3 blots for desmin, Cx43, and CSQ). Protein abundance was normalized to the intensity of the tubulin loading control. Mean values were first calculated for the methodological replicates from the 2-3 independent blots. These values were then used to calculate the overall mean value for each genotype. Results are presented as mean±SEM (relative to wild-type=1).

Action potential (AP) measurements in mouse ventricular preparations. Transmembrane APs were recorded in ventricular preparations from male wild-type and *Zmpste24*$^{-/-}$ mice using glass microelectrodes filled with 3 M KCl (tip resistance: 8-15 MΩ) (13). Multicellular preparations were perfused with a modified Tyrode's solution containing (in mM): NaCl 125, KCl 5.4, $CaCl_2$ 1.8, $MgCl_2$ 1.05, $NaHCO_3$ 24, NaH_2PO_4 0.42 and glucose 11. The solution was bubbled with 95% O_2 and 5% CO_2 (pH=7.4) and maintained at 34°C. The microelectrode was connected with Ag-AgCl wire to high-input impedance, capacity-neutralizing amplifiers (model 701; WPI, New Haven, CT, USA). Left ventricular preparations were stimulated using rectangular pulses (duration 1-2 ms) at a frequency of 3 Hz delivered from a multipurpose programmable stimulator (CS-220; Cibertec SA, Madrid, Spain). APs were computer stored using Acknowledge software. Recordings from at least three stable microelectrode impalements were stored for each preparation.

Intracellular calcium measurements in isolated mouse cardiomyocytes. Ventricular cardiomyocytes were isolated from mouse hearts by enzymatic digestion. Briefly, the heart was mounted on a Langendorf perfusion system and perfused at a constant flow rate of 3 ml/min. The heart was first perfused for 5 min with nominally calcium-free Tyrode's solution containing (in mM): NaCl 88, sucrose 78, KCl 5.4, $MgCl_2$ 1, HEPES 10, Na-pyruvate 5 and glucose 10 plus 2 mg/ml BSA. Subsequently, atria were removed and ventricles were digested for 8 min with nominally calcium-free Tyrode's solution containing collagenase (0.4 mg/ml, Worthington type II). To increase cardiomyocyte yield, additional digestion was carried out for 5 min in collagenase-containing calcium-free Tyrode's solution with gently agitation. This process was repeated three times and desegregated cardiomyocytes were pooled in a solution in which extracellular calcium concentration was increased stepwise to 0.2, 0.4, and 0.8 mM. Cardioyocytes were then stored at room temperature and those showing elongated and striated features were used for electrophysiological, calcium imaging and immunofluorescent labelling studies.

Confocal Ca^{+2} imaging was performed in fluo-4 loaded ventricular cardiomyocytes using a Leica TCS SP5 resonance scanning confocal microscope equipped with a 63X 1.3 NA glycerol objective. Fluo-4 was excited at 488 nm and fluorescence emission was measured between 500 and 650 nm in the frame scanning mode (14). Calcium transients were recorded at room temperature (20-22ºC) and elicited by subjecting cardiomyocytes to electrical field stimulation (5 ms pulses, 5-15 V) at increasing stimulation frequency (0.5 to 4 Hz). Calcium transients and spontaneous calcium waves were automatically detected and quantified using custom-made programs (15).

Perforated patch-clamp in mouse ventricular cardiomyocytes. Ionic currents in ventricular cardiomyocytes were measured with the perforated patch-clamp technique (16). L-type calcium

currents were elicited by a 100 ms depolarization to 0 mV from a holding potential of -80 mV. Na^+-currents were eliminated by inclusion of 30 μM tetrodotoxin in the bath solution and a 50-ms prepulse from -80 to -50 mV. Transient inward currents were measured with the holding potential clamped at -80 mV for 30s. The amount of calcium released from the SR was measured by rapid and transient treatment with 10 mM caffeine (with the membrane potential clamped at -80 mV during the 5 s of caffeine application) followed by integration of the elicited inward current.

Statistical analysis. Data are presented as mean ± SEM. Statistical significance was assessed by unpaired two-tailed t-test for comparisons involving two groups, or one-way ANOVA followed by Newman–Keuls post-hoc test for multiple comparisons. Statistical significance was assigned at $p<0.05$.

REFERENCES

1. Ho D, *et al.* (2011) Heart Rate and Electrocardiography Monitoring in Mice. *Curr Protoc Mouse Biol* 1:123-139.
2. Stypmann J (2007) Doppler ultrasound in mice. *Echocardiography* 24(1):97-112.
3. Monnig G, *et al.* (2006) Electrocardiographic risk stratification in families with congenital long QT syndrome. *Eur Heart J* 27(17):2074-2080.
4. Filgueiras-Rama D, *et al.* (2015) Spectral analysis-based risk score enables early prediction of mortality and cerebral performance in patients undergoing therapeutic hypothermia for ventricular fibrillation and comatose status. *Int J Cardiol* 186:250-258.
5. Priori SG, *et al.* (2013) HRS/EHRA/APHRS expert consensus statement on the diagnosis and management of patients with inherited primary arrhythmia syndromes: document endorsed by HRS, EHRA, and APHRS in May 2013 and by ACCF, AHA, PACES, and AEPC in June 2013. *Heart Rhythm* 10(12):1932-1963.
6. Andersen MP, *et al.* (2008) New descriptors of T-wave morphology are independent of heart rate. *J Electrocardiol* 41(6):557-561.
7. McLerie M & Lopatin AN (2003) Dominant-negative suppression of I(K1) in the mouse heart leads to altered cardiac excitability. *J Mol Cell Cardiol* 35(4):367-378.
8. Mitchell GF, Jeron A, & Koren G (1998) Measurement of heart rate and Q-T interval in the conscious mouse. *Am J Physiol* 274(3 Pt 2):H747-751.
9. Kaese S & Verheule S (2012) Cardiac electrophysiology in mice: a matter of size. *Front Physiol* 3:345.
10. Graff C, *et al.* (2009) Quantitative analysis of T-wave morphology increases confidence in drug-induced cardiac repolarization abnormalities: evidence from the investigational IKr inhibitor Lu 35-138. *J Clin Pharmacol* 49(11):1331-1342.
11. listed Na (1996) Heart rate variability. Standards of measurement, physiological interpretation, and clinical use. Task Force of the European Society of Cardiology and the North American Society of Pacing and Electrophysiology. *Eur Heart J* 17(3):354-381.
12. Schneider CA, Rasband WS, & Eliceiri KW (2012) NIH Image to ImageJ: 25 years of image analysis. *Nat Methods* 9(7):671-675.
13. Caballero R, *et al.* (2010) Flecainide increases Kir2.1 currents by interacting with cysteine 311, decreasing the polyamine-induced rectification. *Proc Natl Acad Sci USA* 107(35):15631-15636.
14. Llach A, *et al.* (2011) Sarcoplasmic reticulum and L-type Ca(2)(+) channel activity regulate the beat-to-beat stability of calcium handling in human atrial myocytes. *J Physiol* 589(Pt 13):3247-3262.
15. Barriga M, *et al.* (2013) Low density lipoproteins promote unstable calcium handling accompanied by reduced SERCA2 and connexin-40 expression in cardiomyocytes. *PLoS One* 8(3):e58128.
16. Hove-Madsen L, *et al.* (2004) Atrial fibrillation is associated with increased spontaneous calcium release from the sarcoplasmic reticulum in human atrial myocytes. *Circulation* 110(11):1358-1363.
17. Li L, *et al.* (2010) A mathematical model of the murine ventricular myocyte: a data-driven biophysically based approach applied to mice overexpressing the canine NCX isoform. *Am J Physiol Heart Circ Physiol* 299(4):H1045-1063.

SUPPLEMENTAL FIGURES

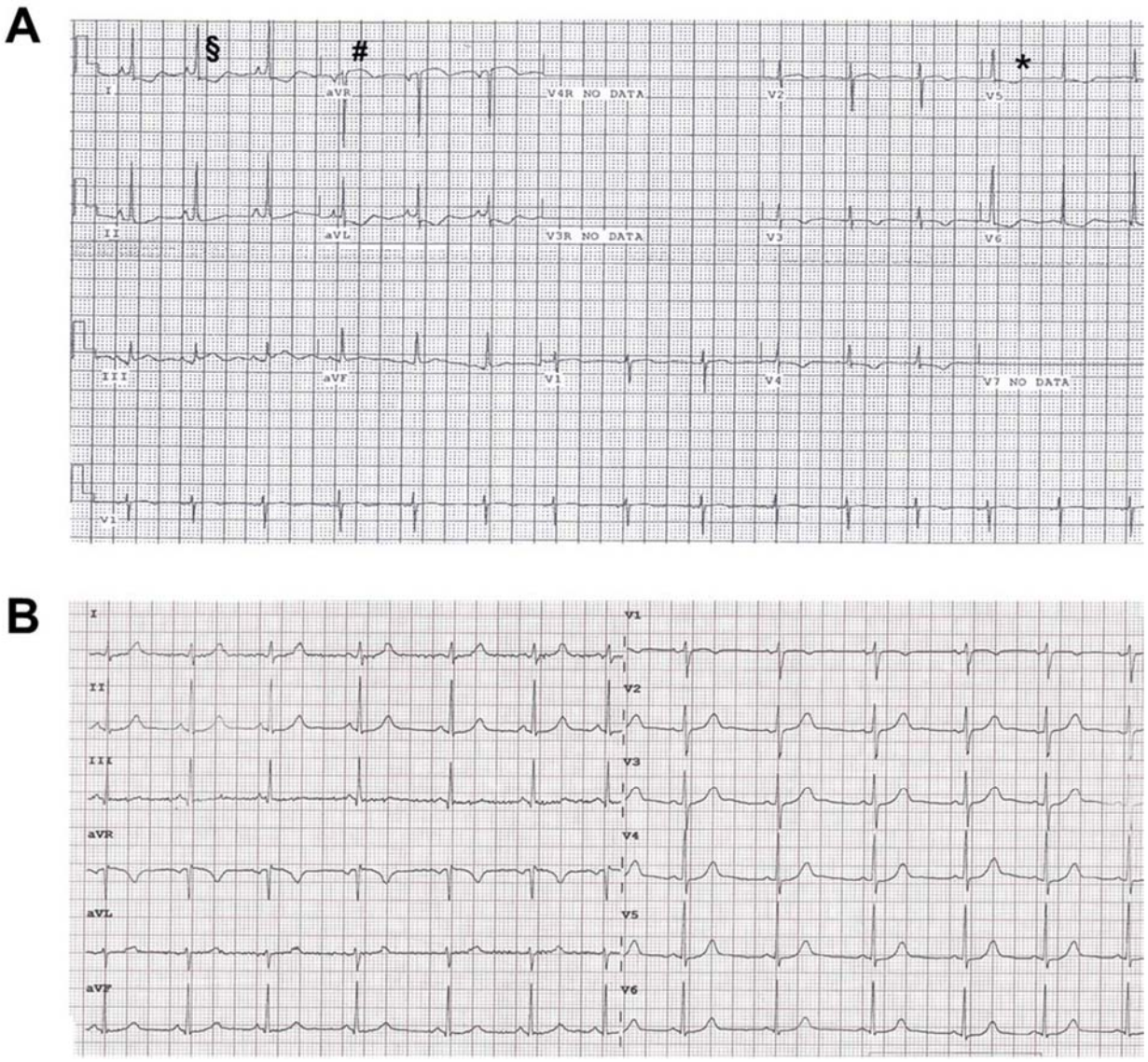

FIGURE S1. Electrocardiogram and rhythm strips in human subjects. Shown are representative 12-lead ECG recordings acquired at 25 mm/s. **(A)** Female HGPS patient (DB296; ECG #6) showing repolarization abnormalities such as negative and biphasic T waves (*), ST depression (§) and ST elevation (#). **(B)** Electrocardiogram tracing from a representative gender and age-matched healthy control (ID1)

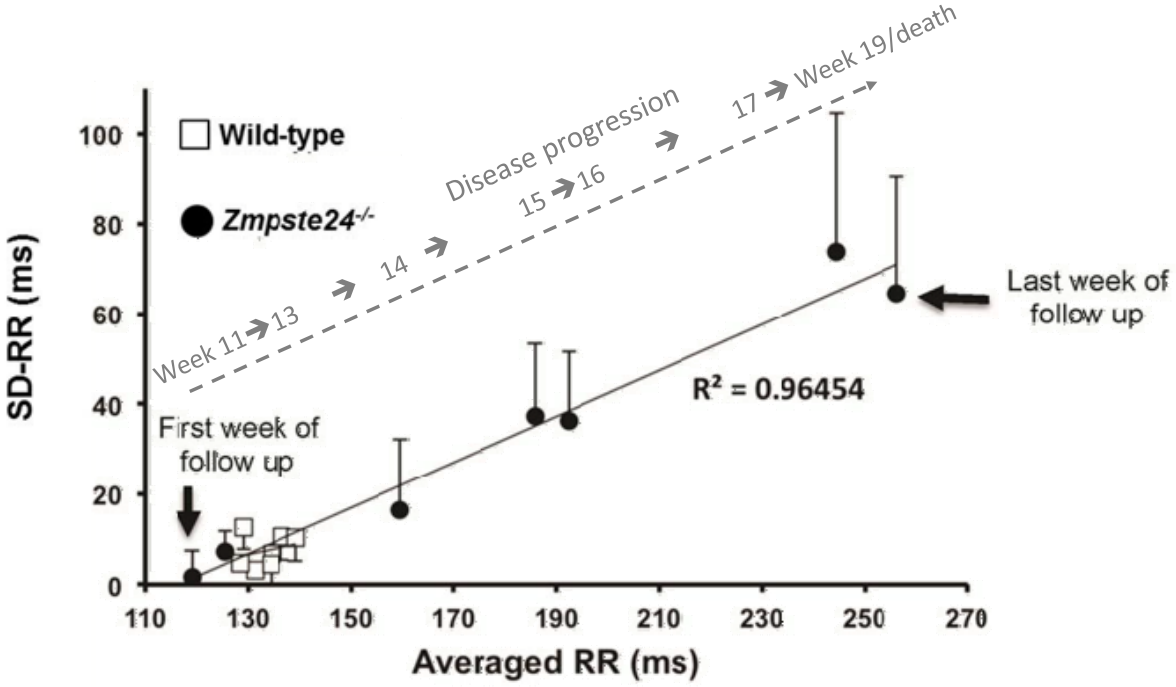

FIGURE S2. Linear increase of the R-R interval from the first to the last week of follow-up in *Zmpste24*$^{-/-}$ progeroid mice. WT and *Zmpste24*$^{-/-}$ mice were given weekly β-adrenergic challenge with isoproterenol starting at 11 weeks of age (First) and until 19 weeks of age or death of the animal (Last). Averaged RR and standard deviation RR (SD-RR) are shown in milliseconds (ms). The discontinuous line shows time progression as disease progresses from first week of follow up (11-13-week-old mice) until week 19 of age or death.

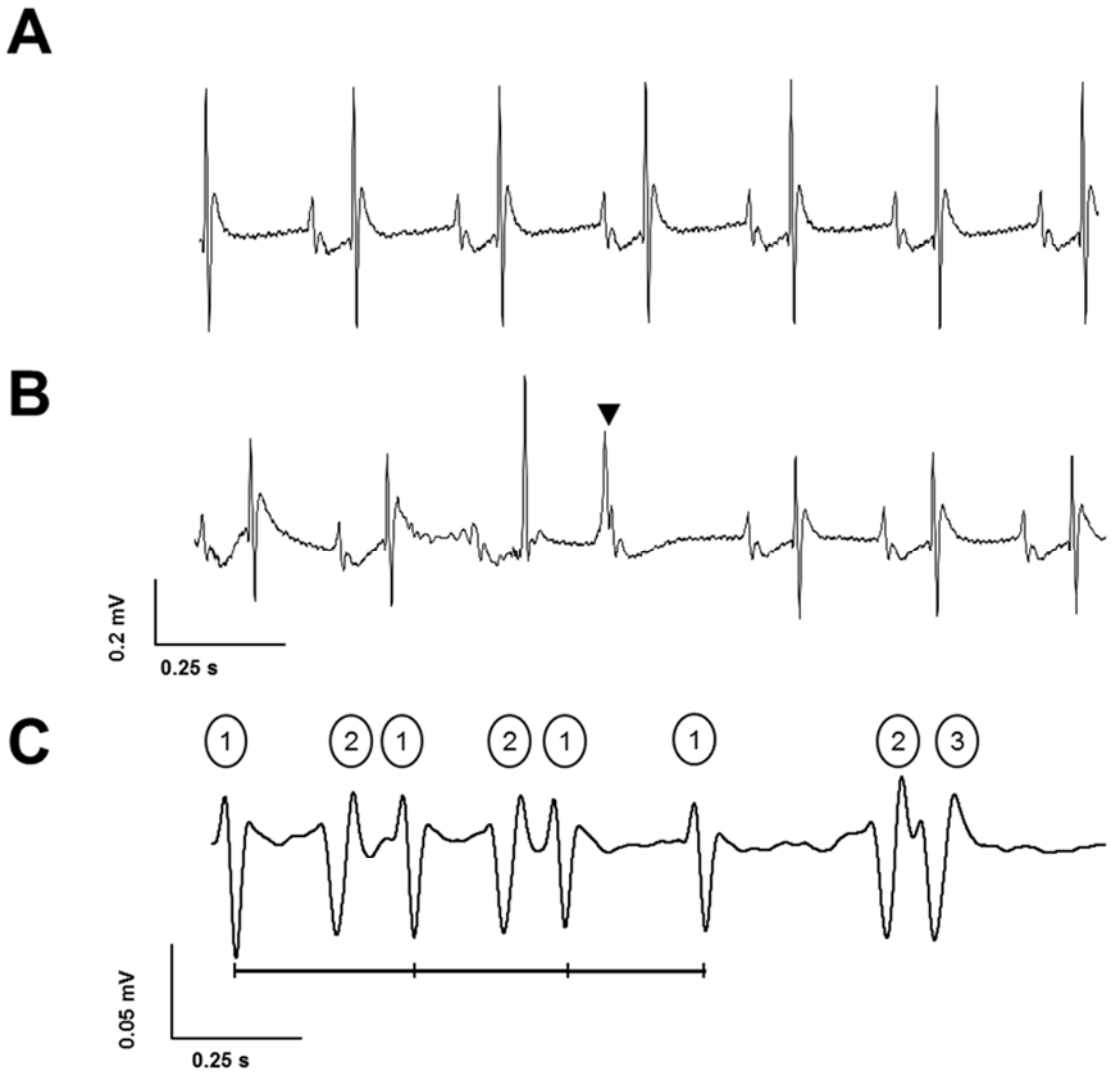

FIGURE S3. *Zmpste24*$^{-/-}$ mice develop premature ventricular complexes (PVC) and slow-rate polymorphic ventricular rhythms. Representative ECG traces and rhythm profiles recorded in lead aVF before **(A)**, after **(B)** and during recovery **(C)** of *Zmpste24*$^{-/-}$ mice from isoproterenol challenge at the last week of follow-up. Arrowhead indicates premature ventricular complexes. Different ventricular morphologies are indicated by numbers. At the beginning of the trace a pseudo-regular ventricular morphology seems to be present.

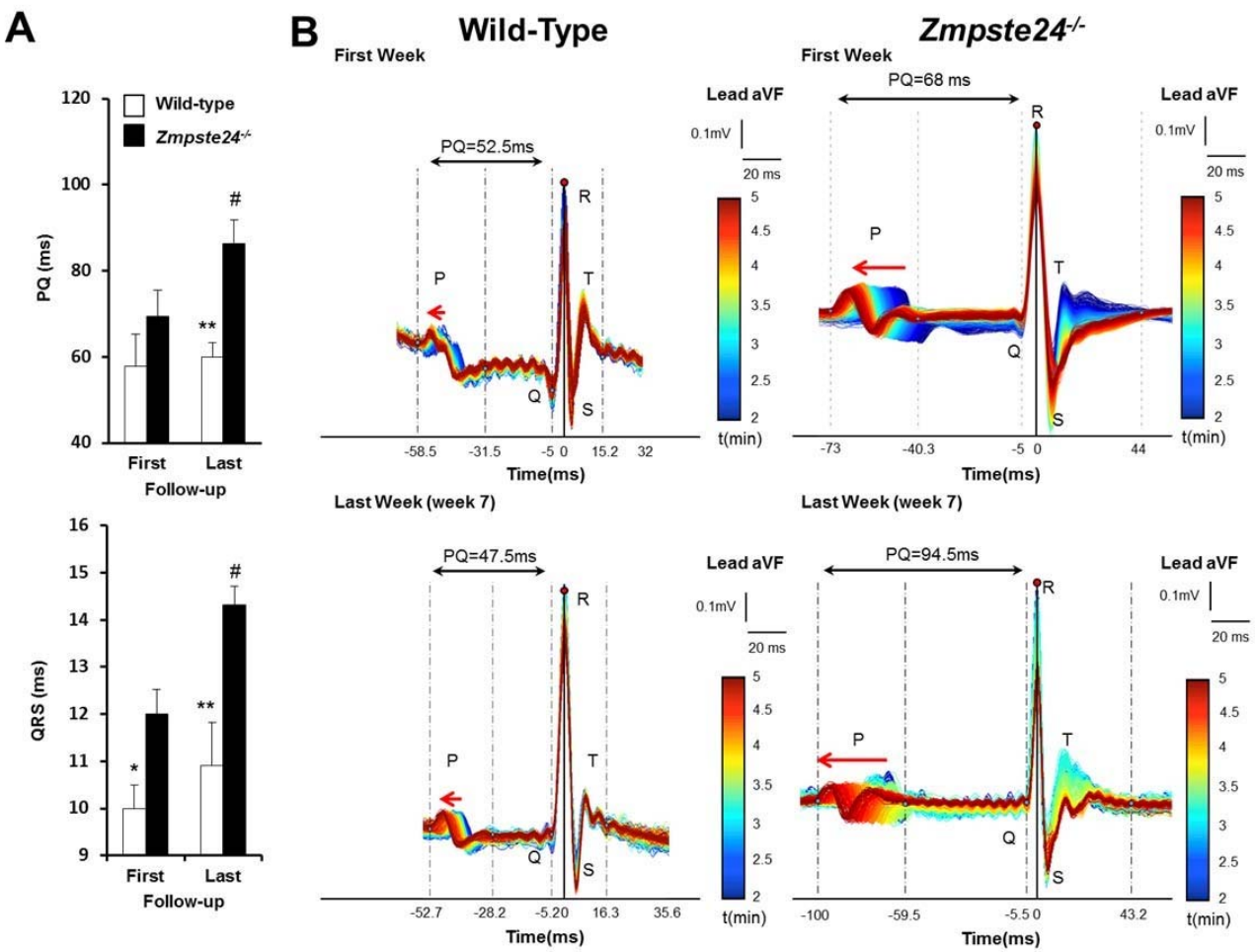

FIGURE S4. PQ and QRS abnormalities observed after isoproterenol bolus. WT and progeroid *Zmpste24*$^{-/-}$ mice were given weekly β-adrenergic challenge with isoproterenol starting at 11 weeks of age (First) and until 19 weeks of age or death of the animal (Last). **(A)** PQ and QRS quantification observed after the first isoproterenol challenge and after the last follow-up challenge. **(B)** Representative superimposed traces color-coded for time from blue to red, illustrating the time course of ECG changes in this period.

*, $p<0.05$; **, $p<0.01$; ***, $p<0.001$ (WT vs *Zmpste24*$^{-/-}$) .

#, $p<0.05$ (First vs Last week of follow-up).

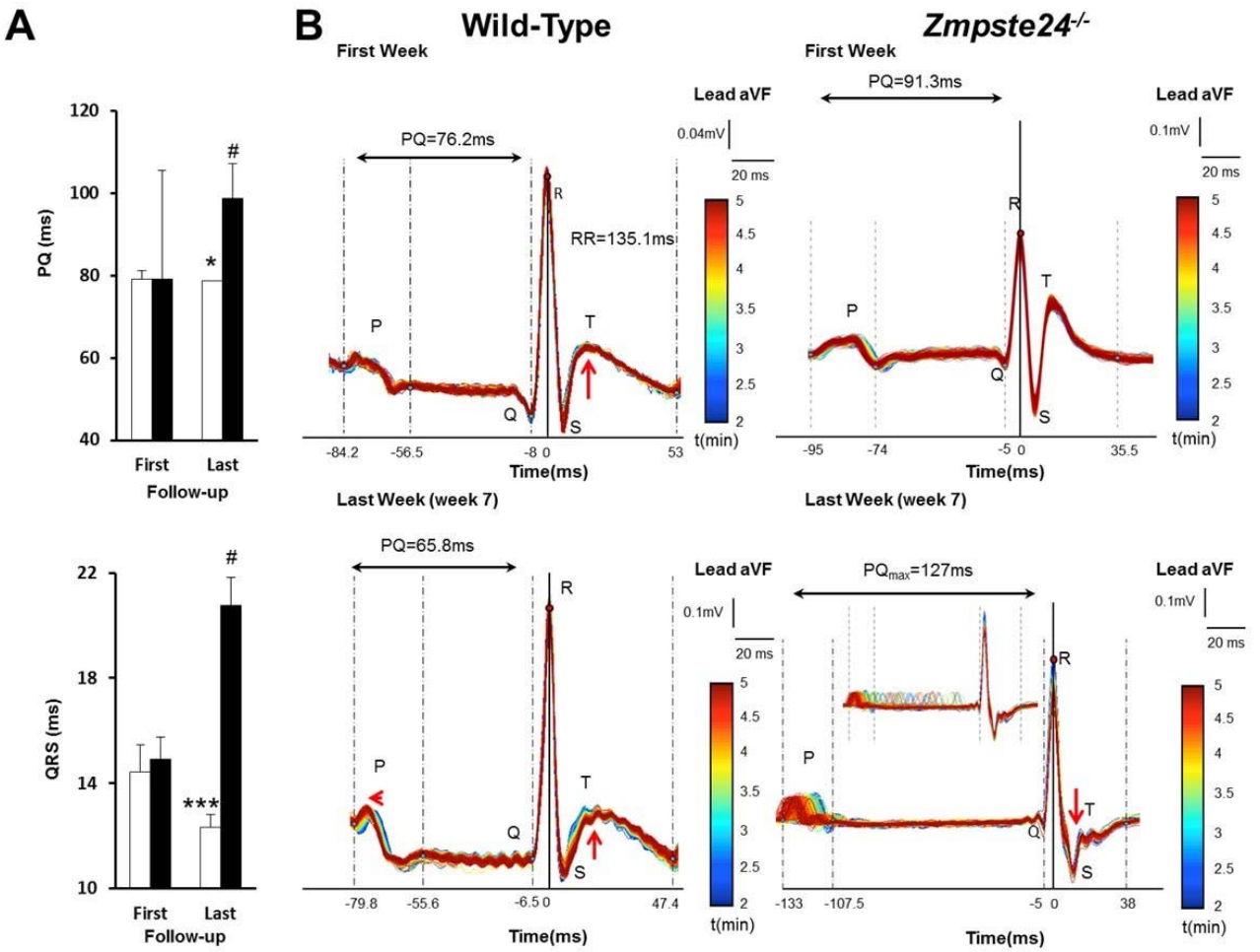

FIGURE S5. PQ and QRS abnormalities observed during recovery from isoproterenol. WT and progeroid *Zmpste24*$^{-/-}$ mice were given weekly β-adrenergic challenge with isoproterenol starting at 11 weeks of age (First) and until 19 weeks of age or death of the animal (Last). **(A)** PQ and QRS quantification observed during recovery after the initial first isoproterenol challenge and the last follow-up challenge. **(B)** Representative superimposed traces color-coded for time from blue to red, illustrating the time course of ECG changes in this period.

*, p<0.05; **, p<0.01; ***, p<0.001 (wild-type vs *Zmpste24*$^{-/-}$).

#, p<0.05 (First vs Last week of follow-up).

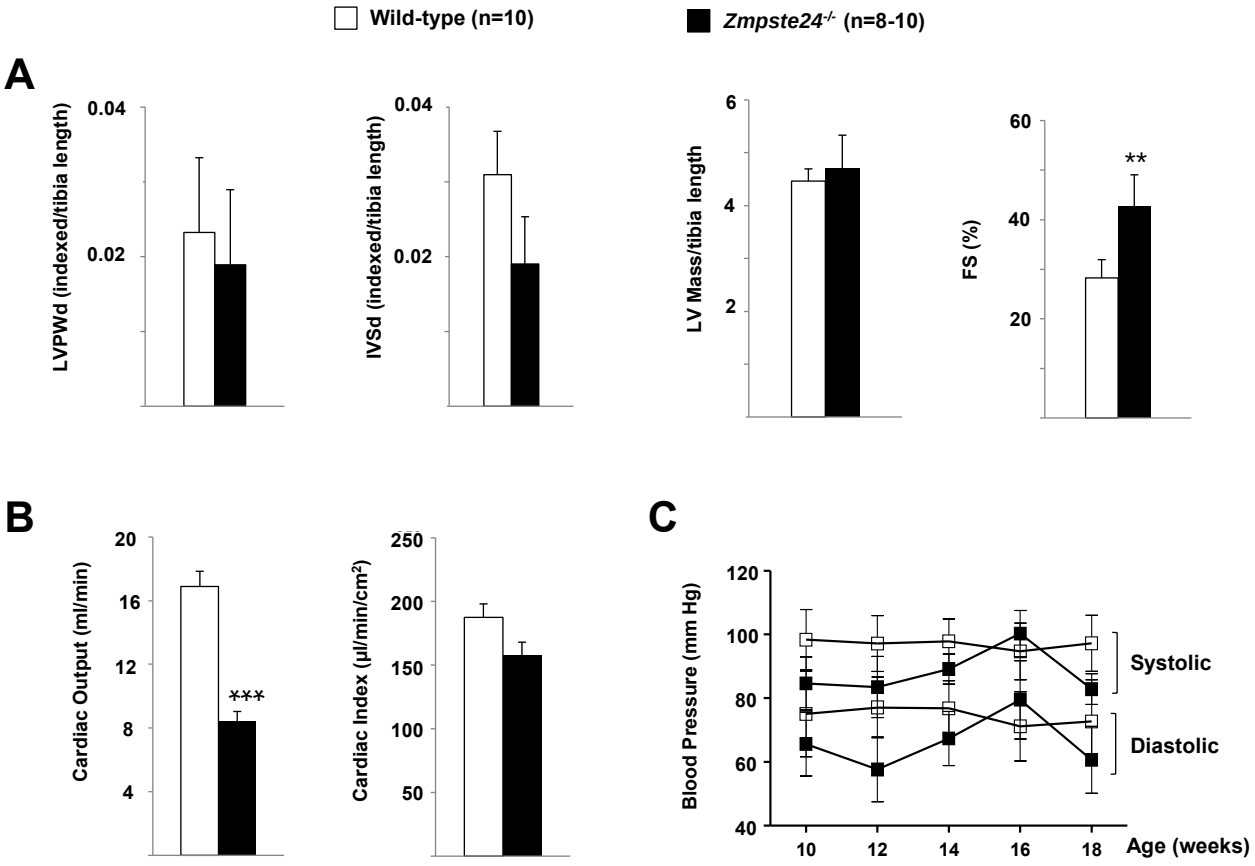

FIGURE S6. Progeroid *Zmpste24*$^{-/-}$ mice have preserved cardiac function and normal blood pressure. (A, B) Mice of both genotypes (18-20 weeks of age) were examined by trans-thoracic echocardiography to quantify LV posterior wall and interventricular septum thickness measured at diastole (LVPWd and IVSd, respectively), and LV mass. All LV parameters were corrected by tibia length. LV function is shown as fractional shortening (FS). Cardiac output (systolic volume x heart rate) and cardiac index (µl/min/cm^2) were also quantified. **(C)** Longitudinal analysis of mice of the indicated ages revealed no differences in blood pressure.

**, $p<0.01$; ***, $p<0.001$.

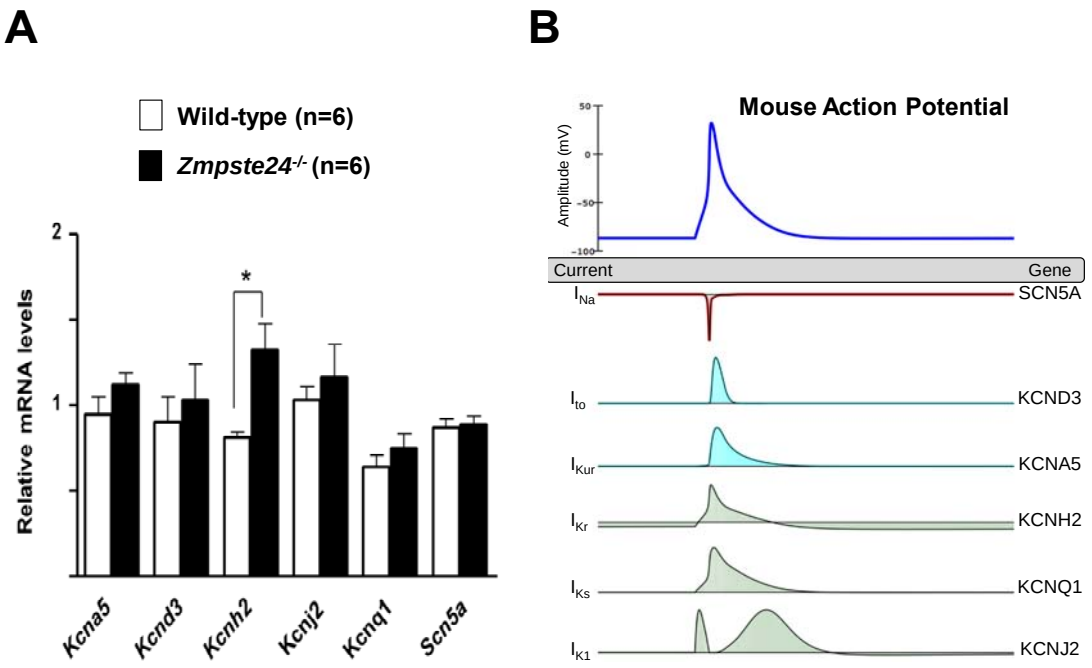

FIGURE S7. Expression of cardiac sodium and potasium channels in WT and *Zmpste24*$^{-/-}$ mice. (A) Real-time qPCR analysis in heart tissue from 16-18-week-old mice to examine mRNA levels of ion channels involved in the different phases of the action potential (see B). The graphs show relative mRNA transcript expression of the indicated sodium channel (*Scn5a*) and potassium channels (*Kcna5, Kcnd3, Kcnj2, Kcnq1, Kcnh2*). Results (Ct values) of triplicate samples from wild-type and progeroid *Zmpste24*$^{-/-}$ mice (n=6 per genotype) were normalized against 18S RNA and are presented as mean±SEM (relative to WT=1). *, $p<0.05$. **(B)** Representative mouse action potential obtained by computer simulation using the validated model reported by Li et al. (17), showing the participating ionic currents and their relation to the genes examined in this study. Elevated *Kcnh2* mRNA levels in *Zmpste24*$^{-/-}$ mice may explain the altered regulation of I_{kr} (rapidly-activated repolarizing potassium current), which might contribute to cardiac repolarization abnormalities.

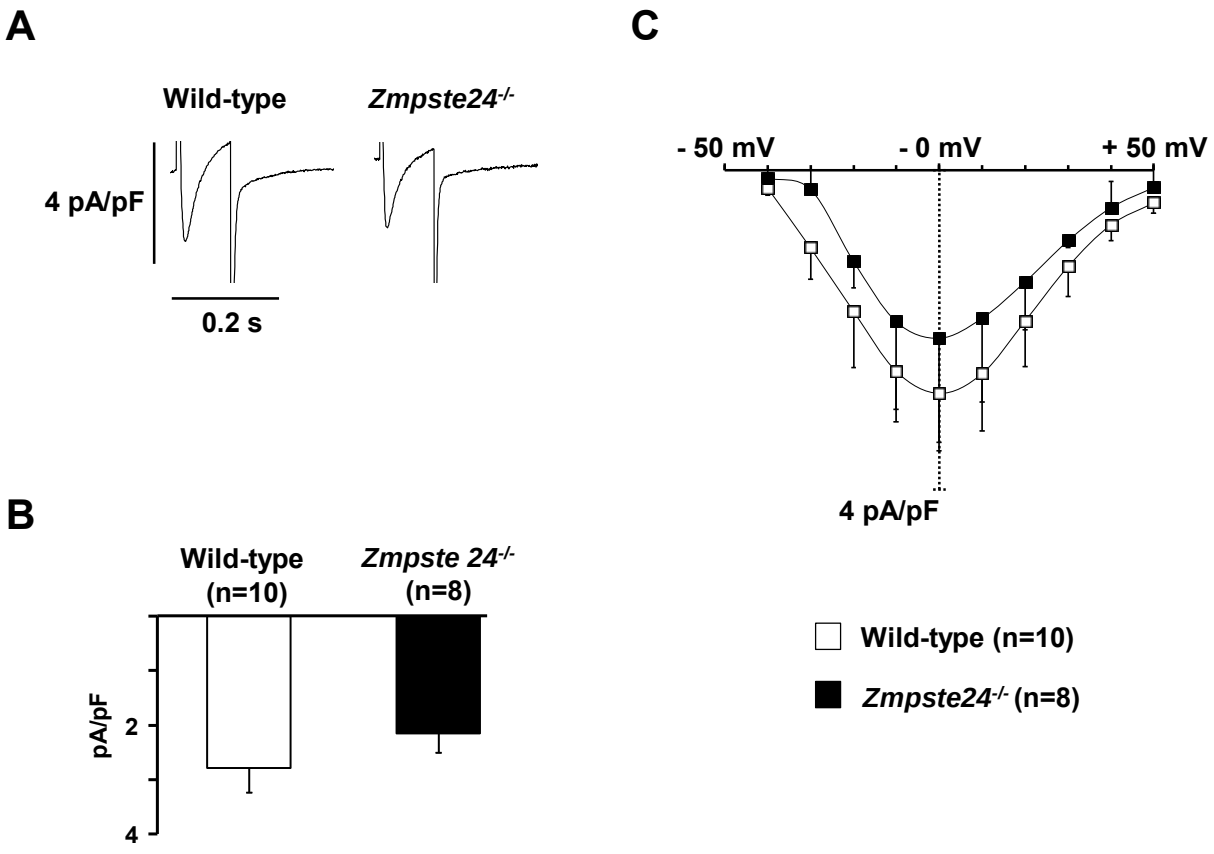

FIGURE S8. L-type calcium current is not significantly altered in *Zmpste24*$^{-/-}$ ventricular myocytes. (A) L-type calcium current traces recorded in myocytes stimulated at 0.5 Hz. **(B)** Average ICa amplitude in isolated myocytes stimulated continuously at 0.5 Hz. **(C)** ICa-voltage relationship recorded in the same myocytes.

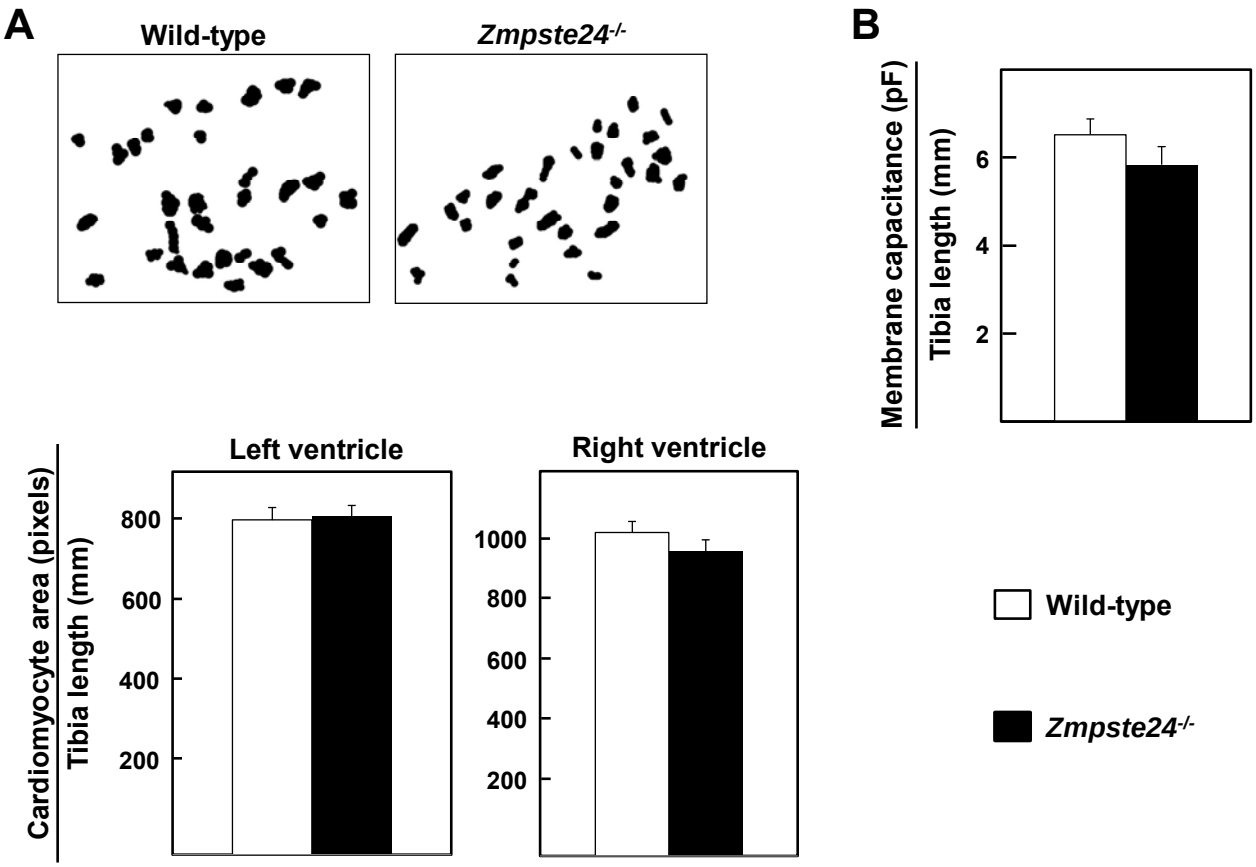

FIGURE S9. Cardiomyocyte size in wild-type and *Zmpste24*$^{-/-}$ mice. (A) Transverse sections of ventricular tissue of WT (n=4) and *Zmpste24*$^{-/-}$ (n=4) mice were stained with Mallory's trichrome or anti-laminin antibodies and digital images were analyzed with Adobe Photoshop to define the profiles of individual cardiomyocytes. **Top:** Representative examples of cardiomyocyte profiles. The total area of each cardiomyocyte cross section (as an estimate of the diameter/minor axis of the cells) was plotted as a black domain on a white background. **Bottom:** The profiles of 90 cardiomyocytes per ventricle (left and right) were analyzed with NIH J software to quantify cell surface (average number of pixels per cardiomyocyte). Graph bars indicate averaged number of pixels per cardiomyocyte normalized by tibia length. **(B)** Membrane capacitance of ventricular cardiomyocytes determined by patch-clamp was normalized by tibia length. Values are from n=23 cardiomyocytes from 10 *Zmpste24*$^{-/-}$ mice and n=39 cadiomyocytes from 12 WT mice. Results were normalized by tibia length because *Zmpste24*$^{-/-}$ mice are significantly smaller than age-matched WT controls. pF: picofarads.

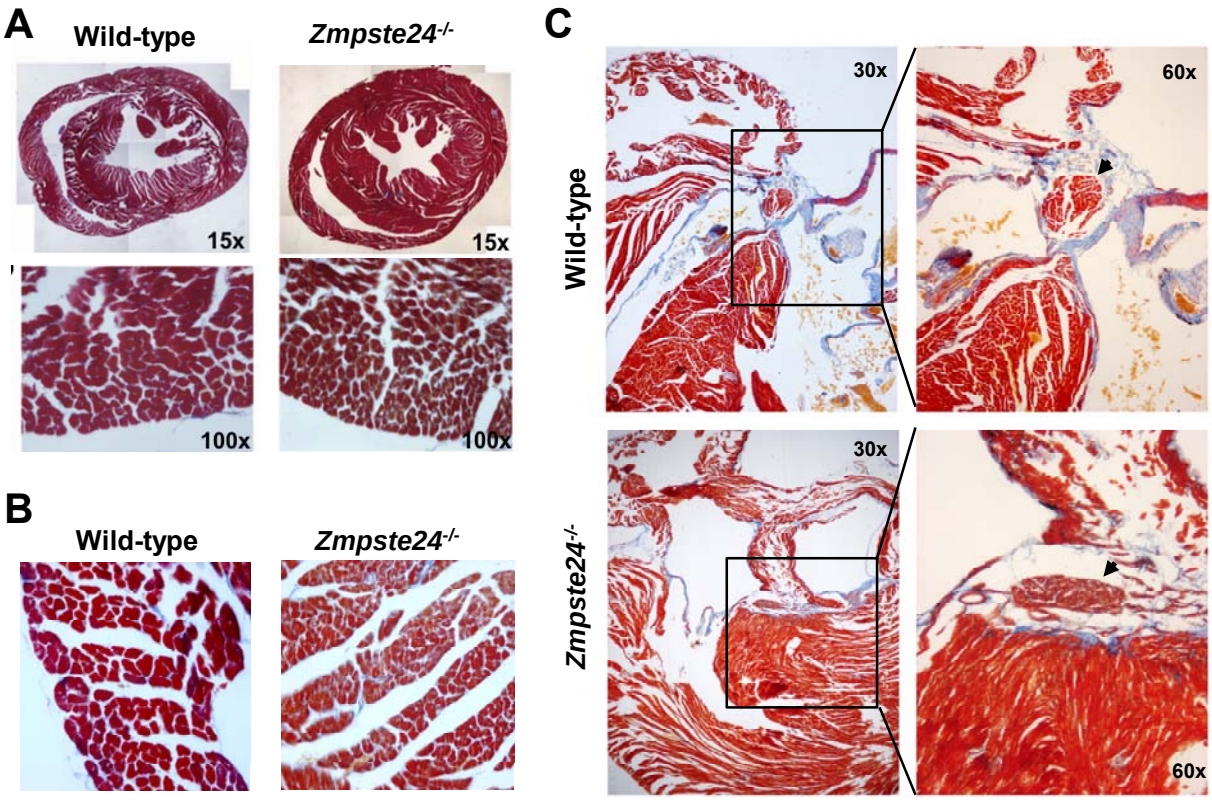

FIGURE S10. Immunohistopathological characterization of the heart of progeroid *Zmpste24*$^{-/-}$ mice. Heart cross-sections from mice at 18-20 weeks of age were stained with Mallory's trichrome. Five mice of each genotype were analysed and representative examples are shown. **(A, B)** Gross examination revealed normal morphology and myocardial fiber arrangement in the progeroid heart. Interstitial fibrosis was negligible in both genotypes. **(C)** Absence of fibrosis in the cardiac conduction system of progeroid *Zmpste24*$^{-/-}$ mice. Magnified views of selected areas are shown. Arrowheads indicate the atrio-ventricular node.

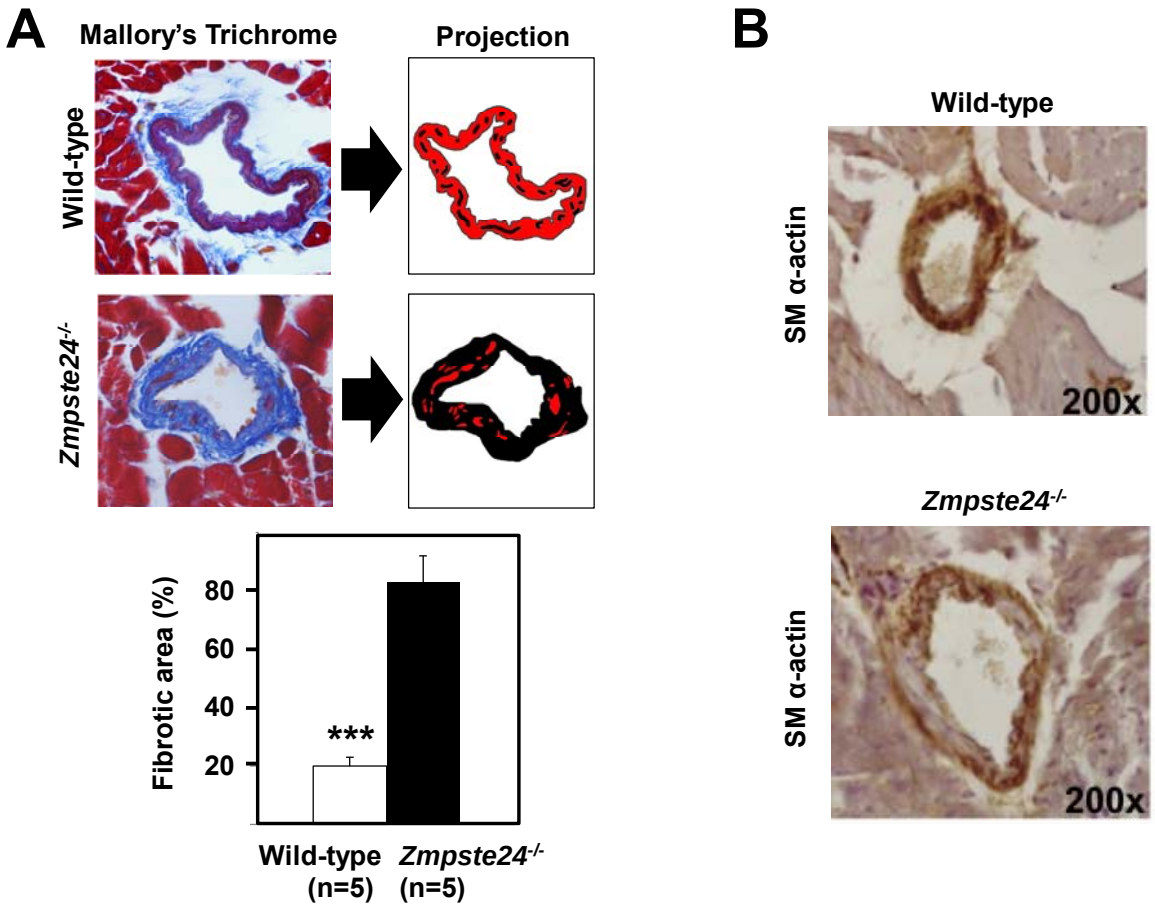

FIGURE S11. Abnormal coronary artery fibrosis in progeroid *Zmpste24*$^{-/-}$ mice. (A) To quantify coronary artery fibrosis, Mallory's trichrome-stained sections were analyzed (n=5 mice of each genotype). Large calibre arteries at the interventricular septum and free ventricular walls were identified and 3 transverse arterial profiles photographed along a total length of 300-400 µm (a minimal distance of 30 µm between sections was observed). Fibrotic and non-fibrotic areas in the vessel wall were projected using Adobe Photoshop (black: fibrotic area; red: non-fibrotic area), and the percentage of fibrotic pixels with respect to the total arterial surface was calculated with FiJi software. **(B)** Loss of smooth-muscle α-actin expression in the major coronary vessels of *Zmpste24*$^{-/-}$ mice.

***, $p<0.001$.

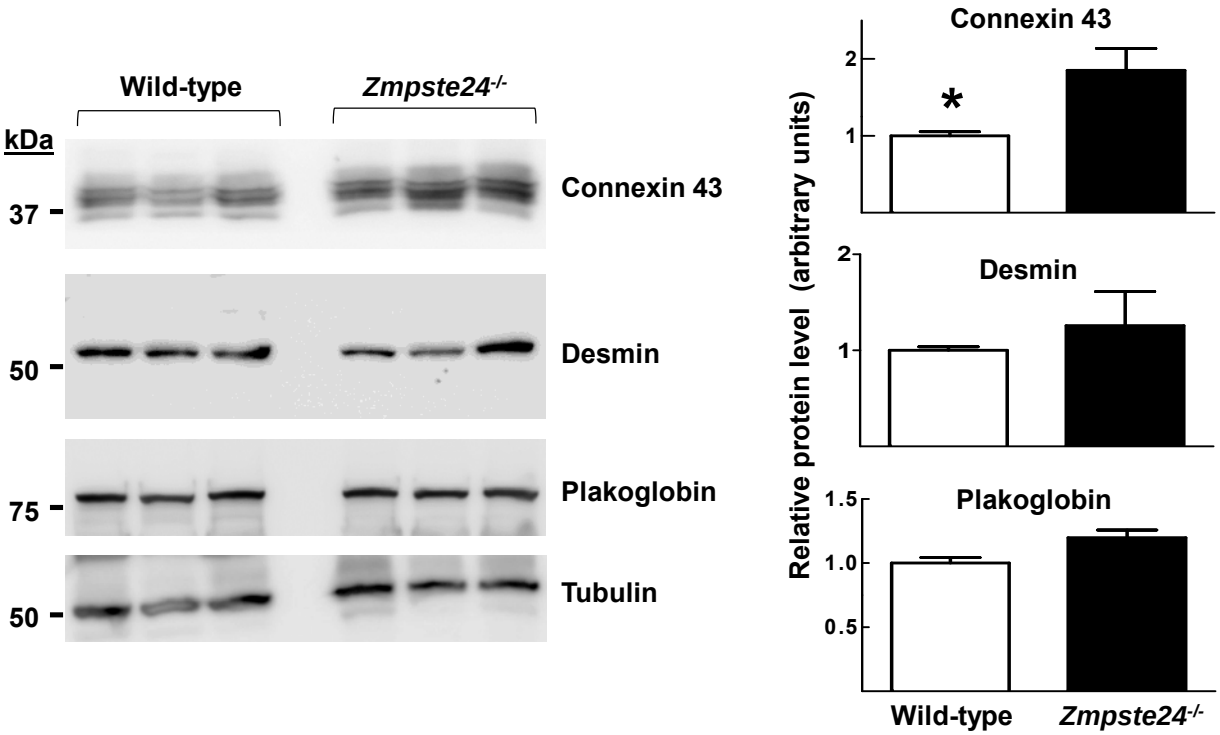

FIGURE S12. Increased expression of connexin 43 in hearts of progeroid *Zmpste24*$^{-/-}$ mice. **(A)** Representative western blots of gap junction proteins (connexin 43 and plakoglobin) and desmosome-interacting protein (desmin) in WT and *Zmpste24*$^{-/-}$ hearts (n=3 per genotype). Tubulin was used as a loading control. **(B)** Quantification of relative protein expression in progeroid mice, normalized to WT.

*, $p<0.05$.

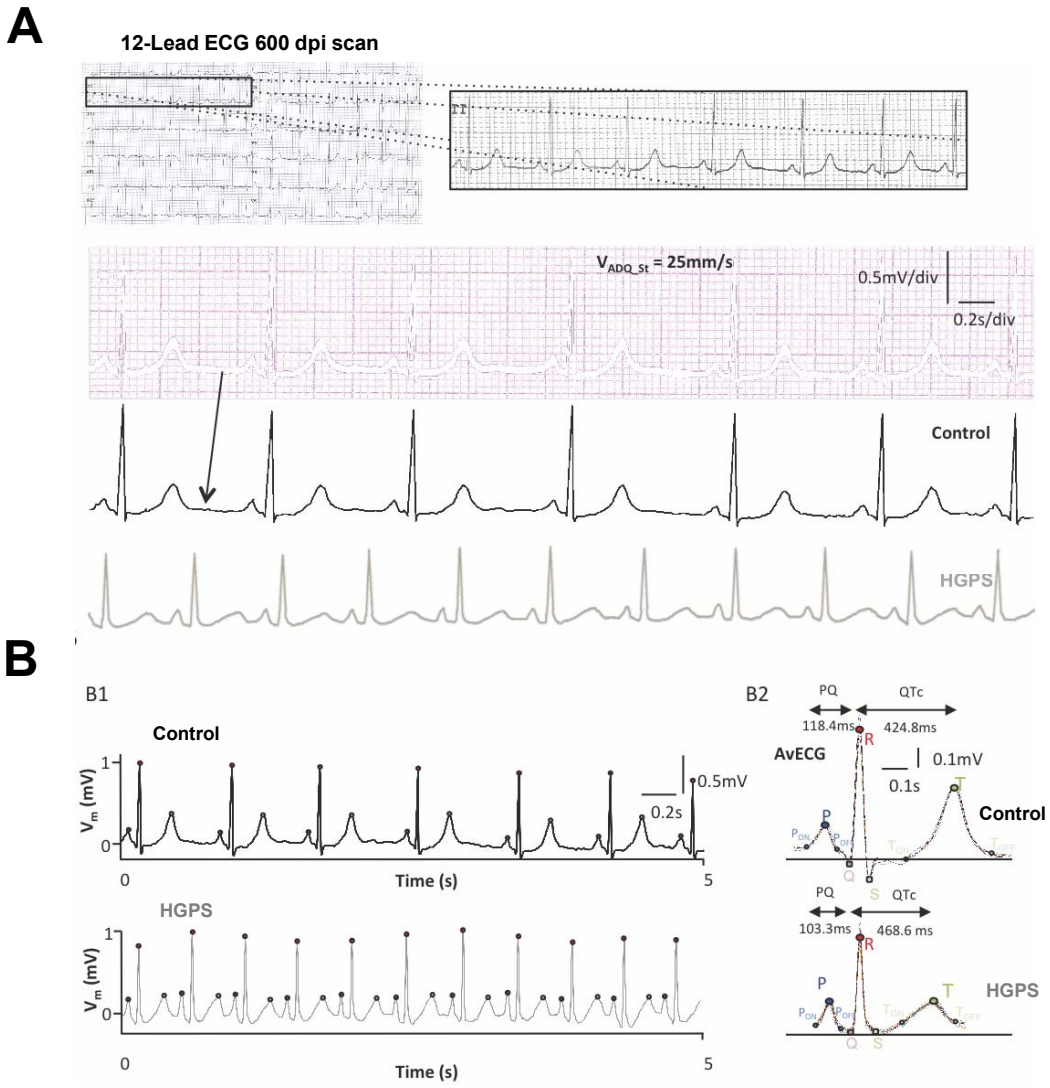

FIGURE S13. Extraction of electrocardiograms in human subjects. Representative 12-lead ECG recordings and extracted lead-II ECG acquired at 25 mm/s (controls in black and HGPS patients in gray). **(A)** Segmented and digitized traces. **(B)** Digitized signal (5-s segments) and averaged ECG calculation for feature extraction.

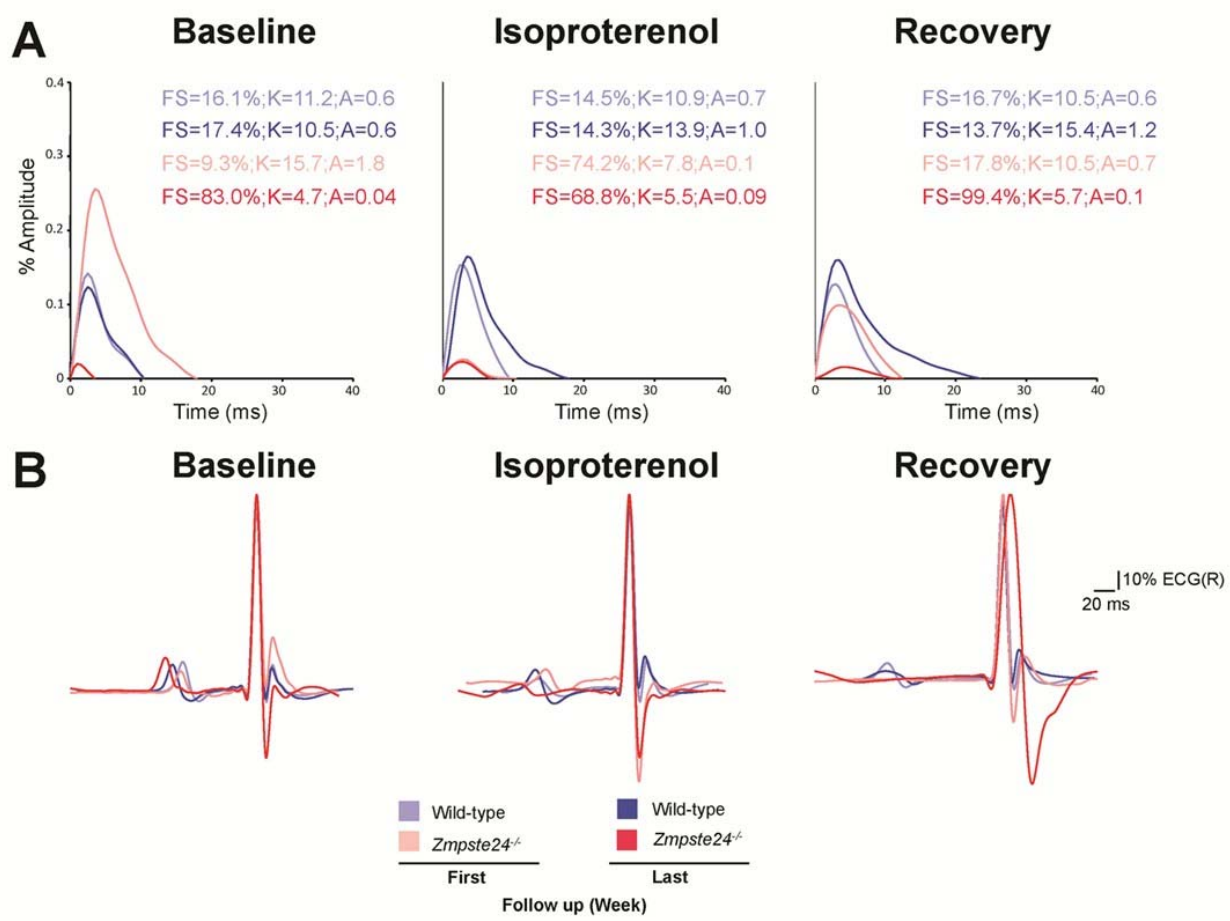

FIGURE S14. Sample measurement for mouse T-wave flattening estimation from normalized signal-averaged ECGs (SAECGs). (A) Segmented T-waves from T-onset to T_{90} and estimated flattening score, kurtosis and area under the T-wave. Increasing values of kurtosis and area under the T-wave correlate with decreasing values of flattening score in each time period. **(B)** SAECG traces obtained at baseline (immediately before isoproterenol), after isoproterenol, and during recovery. WT and *Zmpste24*$^{-/-}$ traces are color-coded in blues and reds, respectively, from light (initial) to intense (last week of follow-up).

TABLE S1. ELECTROCARDIOGRAPHIC MEASUREMENTS IN HGPS PATIENTS

ID	Gender	Age (Year/Month)	Weight (kg)	HR (bpm)*	QRS (ms)§	PR (ms)§	QTc (ms)#	REPOLARIZATION
DB001	**Female**							
ECG1		9Y 10M	11.8	110	74	120	402	Negative T wave V1,V2, aVL; Strain pattern DI
DB053¶	**Male**							
ECG1		13Y 5M	14.06	100	76	110	374	Negative T wave V1, V2, V3, aVL; Strain pattern DI
ECG2		13Y 7M	14.97	117	72	110	406	Negative T wave V1, V2, aVL; Strain pattern V3
ECG3		14Y 8M	14.52	118	72	110	382	Negative T wave V1, V2, V3, aVL; Strain pattern V4
ECG4		14Y 9M	14.97	84	80	115	377	Negative T wave V1, V2, V3
ECG5		15Y 4M	15.88	94	76	120	422	Negative T wave V1,V2,V3,aVL; ST Deppresion (1mm DI, aVL); ST Elevation (1 mm DIII, aVF); QV1-V4
DB060	**Male**							
ECG1		15Y 5M	19.65	88	90	100	388	No repolarization abnormalities
ECG2		16Y 1M	21.85	69	90	110	413	Negative T wave V1; Strain Pattern aVL
DB071	**Male**							
ECG1		16Y 8M	19.5	95	80	140	360	No repolarization abnormalities
ECG2		17Y 8M	18.7	83	80	120	401	ST Depression (2mm V5-V6 (biphasic T wave); 1 mm DI, aVL)
ECG3		17Y 8M	18.7	97	80	120	450	ST Depression (2mm V5,V6 (biphasic T wave); 1 mm DI, aVL)
DB073	**Male**							
ECG1		7Y 2M	9.98	116	70	120	418	Negative T wave V1, V2, V3; Strain pattern V4, aVL
ECG2		7Y 9M	10.21	111	70	125	408	Negative T wave V1, V2, V3; Strain pattern V4
DB100	**Male**							
ECG1		11Y 4M	10.7	107	95	130	428	Q wave DIII
ECG2		11Y10 M	11.57	133	90	125	417	Q wave DIII
DB110	**Female**							
ECG1		6Y 11M	10.9	111	66	116	435	Negative T wave V1, V2
ECG2		7Y 8M	10.5	79	77	120	367	Negative T wave V1, V2
ECG3		8Y 3M	10.9	107	76	120	428	Negative T wave V1, V2, V3; Strain Pattern V4
ECG4		8Y 10M	11	88	76	115	376	Negative T wave V1, V2, V3; Strain Pattern V4
ECG5		9Y 1M	11.2	111	80	120	422	Negative T wave V1, V2, V3; DIII
ECG6		9Y 3M	10.94	88	90	130	412	Negative T wave V1,V2,V3 ; Strain pattern DII
DB113	**Female**							
ECG1		10Y	13.15	150	70	100	395	No repolarization abnormalities
DB118	**Male**							
ECG1		5Y 7M	12.5	150	79	110	427	Negative T wave V1, V2, DII, DIII

ECG2		6Y 4M	11	103	76	125	433	Negative T wave V1,V2, V3; Strain Pattern DIII, V4
ECG3		7Y	11	139	83	125	442	Negative T wave V1,V2, V3, DIII
ECG4		7Y 11M	11.5	79	75	120	379	Negative T wave V1,V2, V3; Strain Pattern V4
ECG5		8Y 5M	11	75	72	120	402	Negative T wave V1,V2, V3, V4, V5
DB120	**Male**							
ECG1		12Y 1M	13.3	115	85	130	388	Negative T wave V1, aVL; Strain Pattern V2
ECG2		13Y 11M	13.3	142	80	120	370	ST Depression (1 mm DI, DIII, aVF; 2 mm DII, V5-V6 (biphasic T wave)); ST elevation (2 mm aVR)
DB136	**Male**							
ECG1		1Y 9M	5.44	136	60	100	347	Negative T wave V1, V2,V3; DIII; Strain Pattern aVF
DB138	**Male**							
ECG1		15Y 11M	17.2	107	90	120	401	Negative T wave aVL; ST Depression (1 mm V4,V5,V6, DI)
ECG2		16Y 1M	18	97	90	130	406	Negative T wave aVL; ST Depression (1 mm V4,V5, DI, aVL)
ECG3		16Y 1M	18	100	90	130	413	Negative T wave aVL; ST Depression (2 mm V4,V5, 1mm V6, DI, aVL)
ECG4		18Y	17.9	133	100	190	537	ST Depression (4 mm V4, V5-V6 (biphasic T wave), 2 mm DI,DII, aVL); ST Elevation (2 mm aVL, V1)
DB145	**Female**							
ECG1		16Y 9M	13.06	107	82	120	401	Strain Pattern V1, aVL
ECG2		17Y 2M	13.22	94	76	120	388	Negative T wave V5, V6; Strain Pattern DIII, aVF, V1, V4
ECG3		18Y 5M	12.93	100	80	120	374	Negative T wave V5, V6; Strain Pattern aVL, V1, V4
ECG4		18Y 5M	12.93	101	80	120	378	Negative T wave V3,V4, V5 ; Strain Pattern aVL, DI,V6
ECG5		19Y	14.15	115	80	130	444	Strain Pattern aVL, aVF, DIII,V4; ST Depression (1mm; V5, V6, DII)
ECG6		19Y 5M	13.64	100	80	120	413	Negative T wave V4, V5, aVL ; Strain Pattern V3, aVF, DI, DII
DB244	**Male**							
ECG1		9Y	10.61	97	72	120	406	Negative T wave V1
ECG2		9Y 4M	10.4	120	72	120	424	Negative T wave V1,V2; Strain Pattern DIII
ECG3		9Y 10M	10.6	130	75	120	398	Negative T wave V1,V2, DIII; Strain Pattern V3
ECG4		10Y 7M	11.1	115	75	120	416	Negative T wave V1,V2; Strain Pattern DIII, V3
ECG5				122	75	120	443	Negative T wave DIII; V1; Strain Pattern aVF
DB296	**Female**							
ECG1		10Y 8M	6.77	127	70	110	462	Negative T wave V1, V3; Strain pattern DIII, aVF
ECG2		10Y 8M	6.77	114	70	100	416	Negative T wave V1, V2; Strain pattern DIII
ECG3		10Y 8M	6.77	112	72	95	440	Negative T wave V1, V2
ECG4		11Y 10M	7.65	133	70	100	472	ST Depression (3 mm V3, V4, V5, V6; 2 mm DI , DII, 1mm DIII); ST elevation (2mm aVR)
ECG5		11Y 11M	7.19	100	70	100	443	Negative T wave V1, V2, V3; ST Depression (1mm V3, V4, V5, V6, DI, aVL); ST elevation (1mm aVL)
ECG6		12Y 5M	7.25	96	70	100	382	Negative T wave V3; V4, V5-V6 (biphasic T wave); ST Depression (1mm DI-DII); ST Elevation (1mm aVR)

* HR: Heart rate (expressed in beats per minute: bpm)

§ QRS, PR and repolarization abnormalities based on age-related changes in pediatrics.

Normal QTc for the adult population is <450 ms and <470 ms in men and women respectively

¶ Denotes overt pathological ECGs

TABLE S2. ELECTROCARDIOGRAPHIC MEASUREMENTS IN HEALTHY CONTROLS

ID	Gender	Age (Years)	Weight (kg)	HR (bpm)*	QRS (ms)	PR (ms) §	QTc (ms)	REPOLARIZATION
1	**Female**	13	61	70	80	115	431	Negative T wave V1; Strain pattern DIII
2	**Female**	7	22	96	70	135	457	Negative T wave V1; Strain pattern V2
3	**Female**	14	64	113	75	100	385	Negative T wave V1,V2,V3
4	**Male**	19	92	59	100	120	396	Negative T wave V1; Strain Pattern aVL
5	**Male**	19	75	59	100	150	376	No repolarization abnormalities
6	**Male**	18	75	67	85	125	392	No repolarization abnormalities
7	**Female**	9	29	67	85	125	390	Negative T wave V1; Strain Pattern DIII
8	**Female**	7	23	74	80	130	389	Negative T wave DIII
9	**Male**	6	20	86	73	140	430	Negative T wave V1,V2; Strain Pattern aVL
10	**Male**	5	19	79	76	113	413	Negative T wave V1
11	**Female**	6	22	87	82	120	421	Negative T wave V1,V2
12	**Female**	8	33	109	80	120	431	Negative T wave V1,V2,V3
13	**Female**	4	18	67	85	120	358	Negative T wave V1

* HR: Heart rate (expressed in beats per minute: bpm)
§ Normal PR is <200 ms
# Normal QTc for the adult population is <450 ms and <470 ms in men and women respectively

TABLE S3. Surface ECG analyses comparing fundamental rhythm parameters between WT and *Zmpste24*$^{-/-}$ mice

	Wild-type (n=6)			*Zmpste24*$^{-/-}$ (n=6)		
Parameters (ms)	**Baseline**	**ISO**	**Recovery**	**Baseline**	**ISO**	**Recovery**
			First week of Follow-Up			
RR	155.85 ± 13.52	131.99 ± 7.23	136.98 ± 4.43	176.73 ± 20.08	136.08 ± 7.22†	210.68 ± 19.89**
PQ	49.16 ± 1.44	57.83 ± 7.36	79.25 ± 4.25†††	53.58 ± 5.03	69.31 ± 6.11†	72.48 ± 19.23†††
QRS	10.80 ± 0.23	10.00 ± 0.48	14.41 ± 1.03††	13.83 ± 1.18*	12.00 ± 0.51*	14.91 ± 0.81
QTc_{90}	25.37 ± 2.07	20.61 ± 1.51†	37.69 ± 5.37	24.61 ± 1.54	24.55 ± 0.56*	25.77 ± 0.91*
			Last week of Follow-Up			
RR	129.73 ± 6.24	119.43 ± 3.47	137.96 ± 2.58	240.37 ± 37.12*	201.41 ± 50.19** ‡	301.59 ± 29.51***‡
PQ	45.66 ± 3.01	60.01 ± 3.34††	78.66 ± 3.78†††	67.41 ± 6.19*	86.34 ± 5.44*** †‡	98.75 ± 8.46* †‡
QRS	10.5 ± 0.32	10.91 ± 0.92	12.33 ± 0.47†	13.9 ± 1.37*	14.31 ± 0.41** ‡‡	20.75 ± 1.07*** ††‡
QTc_{90}	21.83 ± 2.38	22.36 ± 3.19	23.24 ± 4.61	25.52 ± 2.14	24.25 ± 2.03	24.53 ± 2.17

*, P<0.05; **, P<0.01; ***, P<0.001 (Wild-type vs *Zmpste24*$^{-/-}$)

†, P<0.05; ††, P<0.01; †††, P<0.001 (vs Baseline)

‡, P<0.05; ‡‡, P<0.01; P<0.001 (‡ First vs Last week of follow-up)

Mice were given a weekly β-adrenergic challenge with isoproterenol starting at 11 weeks of age (First week of Follow-Up) and until 19 weeks of age or death of the animal (Last week of Follow-Up). Surface ECG analyses comparing fundamental rhythm parameters were performed in anesthetized WT and *Zmpste24*$^{-/-}$ mice at baseline, after adrenergic challenge with isoproterenol (ISO) and during recovery.

TABLE S4. Electrophysiological parameters of transmembrane action potentials recorded ex vivo in ventricular multicellular preparations

Tissue	Mice (n=5)	BCL (ms)	Frequency (Hz)	RMP (mV)	Vmax (V/s)	APA (mV)	APD_{20} (ms)	APD_{50} (ms)	APD_{90} (ms)
Right ventricle	Wild-type	258±31	4.8±0.6	-80.1±1.9	231±10	115.8±2.5	11.6±2.1	35.9±6.2	126±14
	Zmpste24 $^{-/-}$	265±26	4.2±0.5	-77.1±1.2	217±17	117.3±1.9	12.7±1.1	41.3±1.7	120±6
Left ventricle	Wild-type	Stimulated	3	-77.6±1.0	229±3.5	121.5±1.7	9.6±0.7	41.3±1.9	136±7
	Zmpste24 $^{-/-}$	310±24	3.2±0.2	-82.8±2.5	260±7.4	121.2±1.2	13.3±1.2	39.4±2.6	121±5

BCL: Basic cycle length expressed in milliseconds (ms)

RMP: Resting membrane potential expressed in millivolts (mV)

Vmax: Maximum velocity of depolarization

APA: Action potential amplitude

APD: Action potential duration measured at indicated % of repolarization and expressed in ms

(PD-1) blockade. We have developed a mouse tumor model that mimics resistance found in human tumors, and we show that intratumoral injections of a high IFN-inducing CpG oligonucleotide, SD-101, can rapidly lead to durable rejection of anti–PD-1 nonresponder tumors and generate systemic immunity to untreated distant-site tumors. The change in tumor microenvironment caused by SD-101 leads to rapid T-cell infiltration and generation of multifunctional $CD8^+$ T cells. These studies provide significant insights into the synergy between PD-1 blockade and local TLR9 activation and provide the experimental support for clinical studies of combination therapy with PD-1 blockade and intratumoral SD-101. (See pp. E7240–E7249.)

Cardiac electrical defects in progeroid mice and Hutchinson–Gilford progeria syndrome patients with nuclear lamina alterations

José Rivera-Torres, Conrado J. Calvo, Anna Llach, Gabriela Guzmán-Martínez, Ricardo Caballero, Cristina González-Gómez, Luis J. Jiménez-Borreguero, Juan A. Guadix, Fernando G. Osorio, Carlos López-Otín, Adela Herraiz-Martínez, Nuria Cabello, Alex Vallmitjana, Raul Benítez, Leslie B. Gordon, José Jalife, José M. Pérez-Pomares, Juan Tamargo, Eva Delpón, Leif Hove-Madsen, David Filgueiras-Rama, and Vicente Andrés

Defective prelamin A processing causes cardiovascular alterations and premature death in Hutchinson–Gilford progeria syndrome (HGPS) patients and also occurs during physiological aging. We found overt repolarization abnormalities in HGPS patients at advanced disease stages. Similar alterations were present in progeroid *Zmpste24*$^{-/-}$ mice, which had cardiomyocytes that exhibited prolonged calcium transient duration and reduced sarcoplasmic reticulum calcium loading capacity and release, consistent with absence of isoproterenol-induced ventricular arrhythmias. *Zmpste24*$^{-/-}$ mice developed age-dependent bradycardia and PQ interval/QRS complex prolongation, likely contributing to premature death. These defects correlated with mislocalization of connexin43, which was also noted in heart tissue from HGPS patients. These results reveal molecular alterations that might cause cardiac rhythm alterations and premature death in HGPS. (See pp. E7250–E7259.)

Epigenetic gene regulation by Janus kinase 1 in diffuse large B-cell lymphoma

Lixin Rui, Amanda C. Drennan, Michele Ceribelli, Fen Zhu, George W. Wright, Da Wei Huang, Wenming Xiao, Yangguang Li, Kreg M. Grindle, Li Lu, Daniel J. Hodson, Arthur L. Shaffer, Hong Zhao, Weihong Xu, Yandan Yang, and Louis M. Staudt

Autocrine cytokine signaling in cancer can activate members of the Janus kinase (JAK) family, which are generally thought to act by phosphorylating STAT family transcription factors. We report here that JAK1 mediates autocrine IL-6 and IL-10 cytokine signaling in activated B-cell–like (ABC) diffuse large B-cell lymphoma (DLBCL) by a noncanonical epigenetic regulatory mechanism involving phosphorylation of histone H3 on tyrosine 41. We have identified target genes that are activated in ABC DLBCL by this epigenetic mechanism. Knowledge of these epigenetic targets led to our demonstration that JAK1 inhibitors synergize with inhibitors of active B cell receptor signaling in ABC DLBCL, suggesting a new therapeutic strategy for this subtype of DLBCL, which is the most difficult to cure with current therapy. (See pp. E7260–E7267.)

DNA-relay mechanism is sufficient to explain ParA-dependent intracellular transport and patterning of single and multiple cargos

Ivan V. Surovtsev, Manuel Campos, and Christine Jacobs-Wagner

Although intracellular patterning is crucial for cell function, the mechanisms by which spatial patterns arise often remain elusive. Here, we investigate the mechanism of intracellular patterning by the broadly conserved bacterial ParA/B systems, which drive the transport and partitioning of cellular cargos such as plasmids. We show that a simple model that considers only the known biochemical properties of the ParA and ParB proteins and the stochastic dynamics of chromosomal loci observed in vivo explains the spontaneous formation of propagating protein gradients, cargo oscillations, and equidistant patterns that are characteristic of ParA/B systems. Our study shows that stochastic processes and directionally random forces alone—without cytoskeletal elements or motor proteins—can result in directed motion and complex spatial patterning. (See pp. E7268–E7276.)

Mapping human temporal and parietal neuronal population activity and functional coupling during mathematical cognition

Amy L. Daitch, Brett L. Foster, Jessica Schrouff, Vinitha Rangarajan, Itır Kaşikçi, Sandra Gattas, and Josef Parvizi

Humans have the unique ability to perform exact mental arithmetic, which derives from the association of symbols (e.g., "3") with discrete quantities. Using direct intracranial recordings, we measured electrophysiological activity from neuronal populations in the lateral parietal cortex (LPC) and ventral temporal cortex (VTC) that are known to be important for numerical processing as subjects performed various experiments. We observed functional heterogeneity within each region at the millimeter and millisecond scales and report empirical evidence of functional coupling between the LPC and VTC during mathematical cognition. Our results suggest the presence of an anatomically selective numerical cognition system that engages discrete neuronal populations of the ventral temporal and lateral parietal regions in different time windows of numerical processing. (See pp. E7277–E7286.)

Jointly reduced inhibition and excitation underlies circuit-wide changes in cortical processing in Rett syndrome

Abhishek Banerjee, Rajeev V. Rikhye, Vincent Breton-Provencher, Xin Tang, Chenchen Li, Keji Li, Caroline A. Runyan, Zhanyan Fu, Rudolf Jaenisch, and Mriganka Sur

Understanding neurophysiological correlates of neurodevelopmental disorders is one of the pressing challenges of neuroscience. By analyzing a mouse model of Rett syndrome (RTT), we show that cortical pyramidal neurons in methyl-CpG binding protein 2 (MeCP2) mutant mice have reduced excitatory as well as inhibitory synaptic drive. Thus, neuronal response reliability and selectivity, features that arise from excitatory/inhibitory processing circuits within cortex, are reduced. MeCP2 deletion crucially regulates inhibition via two complementary mechanisms: reducing responses of parvalbumin-expressing (PV^+) inhibitory neurons and altering the polarity of GABAergic inhibition in pyramidal neurons. Treating mutant mice with recombinant human insulin-like growth factor-1 (rhIGF1) restores GABAergic polarity along with PV^+ and pyramidal